nature communications

Article

https://doi.org/10.1038/s41467-025-63990-2

A mesothelial differentiation gateway drives fibrosis

Received: 6 April 2024

Accepted: 2 September 2025

Published online: 16 September 2025

Check for updates

Safwen Kadri[1,2,9], Adrian Fischer[2,3,9], Martin Mück-Häusl[1,2,9], Wei Han[2,4,9] ✉, Amal Kadri[2], Yue Lin[2], Lin Yang[1], Shaoping Hu[2], Haifeng Ye[2], Pushkar Ramesh[2], Meshal Ansari[1,5], Herbert B. Schiller[1,5], Hans-Günther Machens[6] & Yuval Rinkevich[7,8] ✉

Internal organs are encased by a supportive epithelial monolayer of mesodermal origin, termed mesothelium. The nature, evolution and function of mesothelial cells, and their genetic regulation impacting disease development are insufficiently understood. Here, we generate a comprehensive organ-wide single-cell transcriptomic compendium of mesothelium across healthy and diseased mouse and human organs, delineating the evolution of conserved activated states of mesothelial cells in response to disease. We uncover genetic drives behind each cell state and reveal a conserved metabolic gate into multipotent proteolytic, inflammatory and fibrotic cell differentiation, in mouse and human. Using lung injury models in mice, in combination with mesothelial cell-specific viral approaches, we show that direct metabolic reprogramming using Ifi27l2a and Crip1 on organ surfaces, blocks multipotent differentiation and protects mouse lungs from fibrotic disease. These findings place mesothelial cells as cellular exemplars and gateway to fibrotic disease, opening translational approaches to subvert fibrosis across a range of clinical indications.

Internal organs and the body cavities, in which they reside, are sheltered in a continuous epithelial monolayer called mesothelium. Mesothelium covers adult organs, whereas during embryogenesis it is known as coelomic epithelium[1]. After birth, the lining of the intestines, stomach and liver are defined as "peritoneal" mesothelium; the lungs and the interior wall of the chest cavity are covered by so-called "pleural" mesothelium and heart and the roots of the great vessels have "pericardial" mesothelium.

Mesothelia provide versatile homeostatic supportive functions to the internal organs and body cavities[1–4]. For example, mesothelia secrete the lubricants that protect organs from external friction or adhesions. Mesothelial cells secrete a carbohydrate-rich glycocalyx across the serosal membranes[3] that coats organ surfaces with a protective barrier[5,6]. Mesothelial cells also receive fluids from the surroundings in a dynamic interchange.

In addition to these homeostatic supportive functions, mesothelial cells have been shown to impact organ immunity, thereby contributing to disease progression and injury-repair. This occurs for example, through expressing inflammatory cytokines and multiple pattern-recognition receptors[7]. The mesothelium also communicates

[1]Research Unit Precision Regenerative Medicine, Helmholtz Munich, Comprehensive Pneumology Center Munich (CPC-M), Member of the German Center for Lung Research (DZL), Munich, Germany. [2]Institute of Regenerative Biology and Medicine, Helmholtz Zentrum München, Member of the German Center of Lung Research (DZL), Munich, Germany. [3]Institute for Diabetes and Cancer (IDC), Helmholtz Munich, German Research Center for Environmental Health, Neuherberg 85764, Germany. [4]Faculty of Medicine, Ludwig-Maximilians-University Munich, Munich, Germany. [5]Institute of Experimental Pneumology, LMU University Hospital, Ludwig-Maximilians University, Munich, Germany. [6]School of Medicine, Department of Plastic and Hand Surgery, Technical University of Munich, Klinikum Rechts der Isar, Munich, Germany. [7]Institute of Regenerative Biology and Medicine, Chinese Institutes for Medical Research, Beijing, China. [8]Capital Medical University, Beijing, China. [9]These authors contributed equally: Safwen Kadri, Adrian Fischer, Martin Mück-Häusl, Wei Han.
✉e-mail: weihan.scientific@gmail.com; yuval.rinkevich@cimrbj.ac.cn

with macrophages and neutrophils, thereby modulating innate immune cell influx across serosal membranes and into the organs[8–11]. Mesothelia also produces growth factors and extracellular matrix (ECM) components[12–14]. This allows mesothelial cells to contribute to fibrosis progression across a variety of internal organs and cavities, including myocardial infarctions[15–17], heart repair[18,19], CCL4-induced liver fibrosis[20], lung fibrosis[21,22] and abdominal adhesions[23,24].

Despite indications that protective and deleterious functions of mesothelial cell states are clearly tightly linked to organ disease responses, mesothelial cells remain outside from current mainstream/accepted paradigms of mammalian and human fibrosis. This is due in part to lack a comprehensive understanding of mesothelial cells in health and disease, and lack of tools/methodologies to explore their function in living mammals. Understanding the mechanism of how mesothelial cells choreograph and switch the response to disease and repair injury, promises enhanced wound healing and the subverting of fibrotic disease across a arrange of human clinical indications.

Here, we generate comprehensive transcriptomic atlases of thousands of individual mesothelial cells across mouse and human organs and pertinent diseases. We discover universal supportive and disease-specific cell states, across many organs, in a conserved multipotent differentiation trajectory in lining mesothelium, starting with a crucial metabolic priming commitment event. This differentiation cascade dictates and choreographs disease responses through specific genes driving the sequential differentiation between each mesothelial cell state in the run-up to fibrosis. Our schema of mesothelial cell states and functions presented here thus opens therapeutic opportunities for the prevention and treatment of organ diseases.

Results

A mesothelial cell compendium across healthy mouse organs

To obtain a detailed panoramic view of mesothelial cell states across mouse internal organs, we compiled and re-analyzed 32 single-cell RNA-seq datasets from public repositories across twelve different tissues/organs including lung, heart, liver, spleen, mesentery, kidney, pancreas, adipose tissue, uterus, vasculature, prostate and omentum—generating a compendium of 23,134 mesothelial cells. When available, we used pre-processed data and extracted mesothelial cell datasets based on the authors' annotation. When annotation was unavailable, we used raw data, which we preprocessed, filtered, and annotated, using restricted criteria of defined mesothelial markers. We also excluded immune, endothelial, and epithelial cell types. We then corrected our compiled dataset for any batch effects using BatchBench[25] before merging, filtering, normalizing (Fig. 1a and Supplementary Fig. 1a).

We then performed dimension reduction UMAP analysis, followed by Leiden analysis (resolution = 0.5), which revealed eight distinct mesothelial cell clusters. We annotated these according to their most distinguishing gene's expression: Cadherin 12 (Cdh12), Sodium Leak Channel Non-Selective (Nalcn), Prothymosin Alpha (Ptma), Delta Like Non-Canonical Notch Ligand 1 (Dlk1), Dermatopontin (Dpt), Mitochondrially Encoded Cytochrome C Oxidase I (Cox1), Thymosin Beta 10 (Tmsb10) and Actin Gamma 1 (Actg1) (Fig. 1b).

Each of these eight mesothelial cell types, expressed unique transcript profiles with over 200 differentially expressed genes. When comparing the tissues origins of the groups we found they had distinct organ-distributions with organ-specific expression pattern. Some of the cell types were found in a unique organ, whereas others were globally present across different organs. For example, adipose tissue and lung cells, contain organ-specific mesothelial subsets (Supplementary Fig. 1b).

Lung mesothelium was more complex, including two different mesothelial cell types, distinguished by expression of Ptma and Cox1. Indeed, immunostaining on healthy mouse lung samples confirmed both subtypes were present (Supplementary Fig. 1c). Interestingly, the Ptma group of cells also overexpress infectious disease and innate immune response genes and those involved in cellular responses to stimuli. As with lung adipose tissue was composed of two different cell types expressing either Cdh12 or Nalcn. Gene ontology (GO) enrichment indicated Cdh12 cells are involved in regulation of macromolecule biosynthesis process, cell projection organization, cellular response to stress and cytoskeleton organization, whereas Nalcn cells are involved in immune response and cellular responses to stimuli (Supplementary Fig. 1d).

Our analysis further identified two multi-organ mesothelial cell types. The first expressed Tmsb10 and was present across many different organs such as prostate, uterus, spleen, heart, and vascular. Tmsb10 plays an important role in cytoskeletal organization by binding to actin monomers, suggesting a role for this mesothelial cell type in organ surface rigidity. The second multi-organ mesothelial cell type overexpressed Actg1 and was specific to abdominal organs including liver, kidney and omentum. Actg1 is a non-muscular cytoskeletal actin isoform that regulates cell proliferation, apoptosis and tumor cell migration.

We then employed "pseudotime" analysis to determine the hierarchical "distance" between the mesothelial cells from different tissues. Our analysis indicated mesothelial cells within individual body cavities (either pericardial, pleural or peritoneal) share gene expression patterns, have a closer hierarchical distance, and have a more recent common cellular ancestor than mesothelial cells from adjacent cavities (Fig. 1c and Supplementary Fig. 1e, f).

A mesothelial cell compendium across mouse diseased organs

Next, we extended our analysis to diseased tissues and organs. For a deep dive into the different mesothelial cell states and their potential functions in disease, we collected mesothelial cell scRNA-seq data from twenty-five mouse datasets representing seven different fibrotic-related diseases, including lung and liver fibrosis, heart and kidney ischemia, heart aortic constriction, pancreatic adenocarcinoma, peritoneum adhesion, vasculature high fat diet. This revealed three new disease-specific cell states (Fig. 1d).

We determined the most enriched signaling pathways in each state, using reactome pathway analysis, and annotated these three mesothelial cell states as (i) a "fibrogenically-active" cell state expressing pathways for collagen biosynthesis and its modifying enzymes, (ii) a "metabolically-active" state expressing metabolic pathways of amino acids and derivatives, and (iii) a "proteolytically-active" state related to connective tissue dismantling, including matrix metalloproteinases and collagen degradation enzymes (Supplementary Fig. 1g–j). These three cell states were universal, appearing across many diseases, animal models and organs (Fig. 1e). We further identified distinguishing markers for each cell state, including Matrix Gla protein (Mgp) and Secreted Protein Acidic and Cysteine Rich (Sparc) for "fibrogenically active", interferon alpha-inducible protein 27 like 2A (Ifi27l2a) and Cysteine Rich Protein 1 (Crip1) for "metabolically-active" cells and Decorin (Dcn) and Placenta Associated 8 (Plac8) for "proteolytically-active" cells (Fig. 1f).

Lung fibrosis is driven by mesothelial cell state differentiation

To determine the interrelationships between the three universal mesothelial cell states across a disease progression timeline, we analyzed scRNA-seq of mesothelial cells from a Bleomycin-instilled lung fibrosis model, using eighteen different time points spanning 54 days (Fig. 2a). This lung fibrosis progression analysis revealed the same three cell states with the same markers as before: (i) fibrogenic, (ii) metabolic, and (iii) proteolytic with the addition of a fourth (iv) "immune modulatory" state with Serum Amyloid A3 (Saa3) as marker (Fig. 2b, c). This fourth cell state was enriched for interleukin and cytokine signaling and other immune system pathways (Supplementary Fig. 2a–g).

https://doi.org/10.1038/s41467-025-63990-2

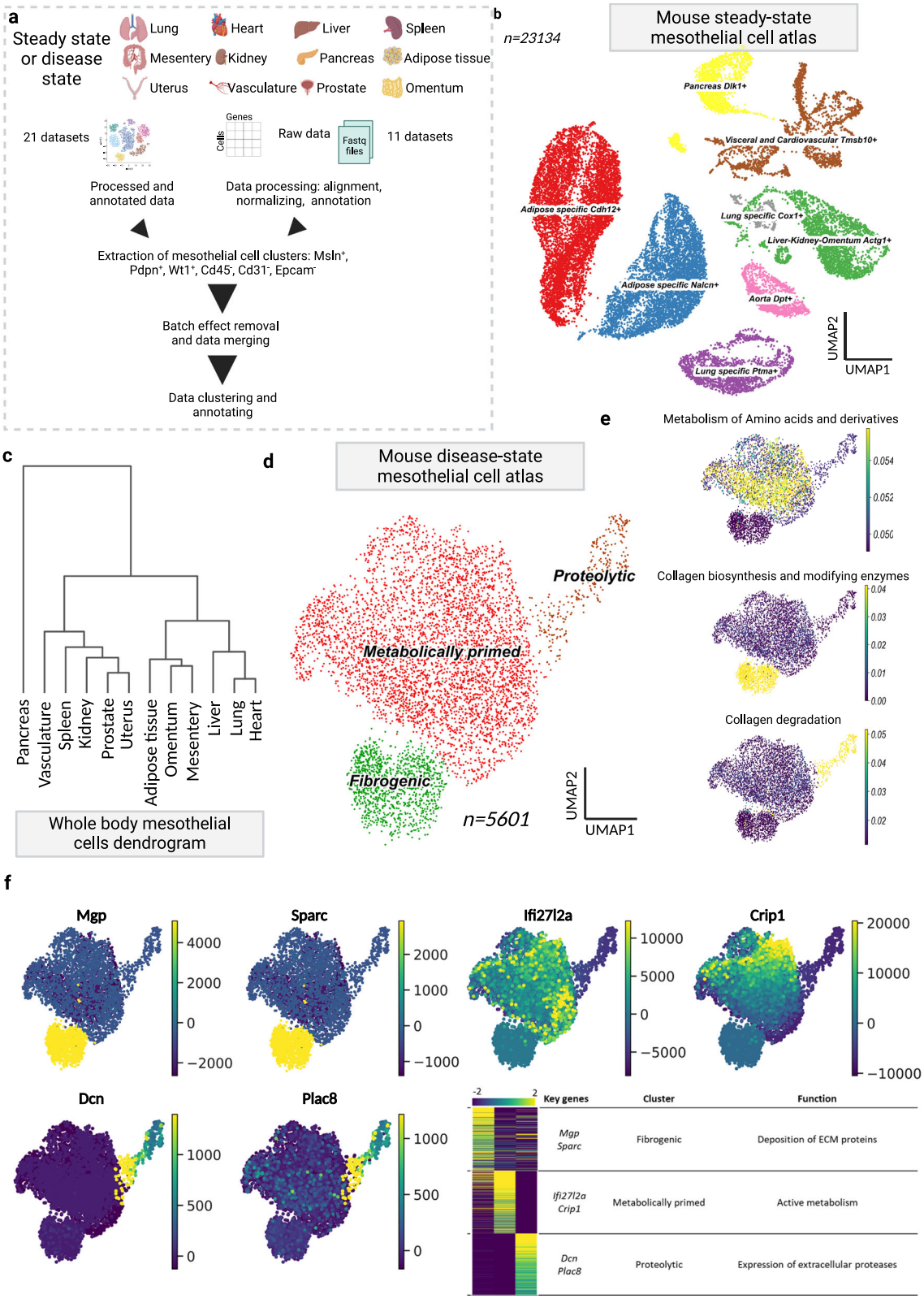

The earliest disease-specific mesothelial state was predicted to be metabolically active cells expressing Ifi27l2a, and Crip1. Metabolically active cells were predicted to differentiate into proteolytic-active cells overexpressing metalloprotease and endopeptidases, including Matrix Metallopeptidase 8 and 14 (Mmp8, Mmp14) Cathepsin B (Ctsb), Dcn and Plac8. Proteolytic cells transiently were predicted to differentiate into immune-active cells expressing chemoattractant Saa3. Finally, immune modulatory cells were predicted to differentiate into fibrogenically active cells, overexpressing Mgp, Sparc and collagens 1 and 3 (Fig. 2d and Supplementary Fig. 2g). This unprecedented differentiation pathway is likely key to the fibrotic process.

The predictive differentiation steps were mirrored by sequential enrichment of the mesothelial cell states over the time-course. For

Fig. 1 | Steady-state and disease mouse mesothelial cell atlas. a Schematic representation of the experimental procedure for the generation of the healthy state mouse mesothelial cell atlas. Thirty-two single cell datasets of healthy mouse mesothelial cells in twelve different organs were collected and integrated for the single-cell atlas generation. Preprocessed data and raw data were processed, annotated and then we extracted the mesothelial cells cluster based on the expression of Msln, Pdpn, Wt1 and the absence of Cd45, Cd34 and Epcam. Batch effect was then removed, and datasets were merged and analyzed. **b** UMAP embedding of 23,134 single cells in the steady-state atlas. The eight clusters identified through graph-based clustering are labeled with the most discriminative gene and indicated by different colors. **c** Hierarchical clustering of the different mesothelial cells, depending on the tissue of origin showing the hiearchy of the mesothelial cells in the different tissues. **d** UMAP embedding of 5,601 single cells in the mesothelial disease-state atlas. The three clusters identified through graph-based clustering are indicated by different colors. **e** UMAP embedding of the mesothelial disease-state atlas color coded with the expression of the highest enriched reactome terms. **f** Gene markers of the different disease states of the mesothelial cells. UMAP of mouse disease state mesothelial cell atlas, color coded for the different cluster markers. On the left bottom, is a heat map of the relative average expression, of the most strongly enriched genes for each cluster in the mesothelial disease state atlas (log(fold change), of one cluster versus all others. Created in BioRender. Kadri, S. (2025) https://BioRender.com/2qncy1b.

example, mesothelial cells adopted a metabolically active phenotype in the initial pre-fibrotic period from day 2 until day 6 of the Bleomycin model. On day 7 after Bleomycin installation these metabolically active cells differentiated into proteolytic cells, and the two cell types co-existed within the lung pleura until day 10 when some proteolytic cells adopted immune modulatory phenotypes. This immune phenotype emerges around day 5 and gradually increases, reaching its peak at day 10. Then, these immune modulatory cells transition progressively into fibrogenic cells, coinciding with the onset of lung fibrosis at day 11. Starting from day 21 fibrogenic cell numbers plummet, reverting to metabolically active cells, which coincides with fibrosis resolution (Fig. 2e). We confirmed the temporal appearance of these four cell types on sections from fibrotic mouse lungs across day 0, 5, 10, and day 14 (Supplementary Fig. 3).

Next, to identify the genetic regulation of this cell state differentiation, we estimated fate probability and analyzed driver genes across all mesothelial cell states, using the CellRank package[26,27]. We identified the same drive genes between the cells states in disease as we had observed in our cross-tissue analysis above including the metabolic driver Ifi27l2a, Dcn and Plac8 controlling proteolytic differentiation, Saa3 driving Immune modulatory differentiation, and Mgp, and Sparc are at the apex of fibrogenic differentiation (Fig. 2f).

Mesothelial differentiation triggers pathological matrix internalization

To functionally explore the role of these drivers, ex vivo, we overexpressed individual cell state drivers on pleural lung surfaces. Transfection was made possible with a specialized AAV capsid containing an RGD motif on its viral coat, enabling immediate binding and internalization of the AAV into pleural lining cells. Our AAV strategy contained the genetic driver under the control of a CMV promoter, to force a strong and constitutive expression on pleural surfaces, as well as an mCherry reporter tag, to visualize and quantify transfection/transduction efficiency. To directly assess proteolysis and surface material transfer, we tagged pleural ECM with Fluorescein Isothiocianate (NHS-ester), and 300 μM thick slices were incubated with medium for 5 days then immunolabeled and visualized with confocal microscopy (Fig. 3a).

Overexpression of the above drivers induced a robust differentiation of lining mesothelium ex vivo. Overexpression of Ifi27l2a increased metabolism and mitotic activity, evidenced by increased Ki67 and PCNA staining (Supplementary Fig. 4a). Overexpressing Dcn and Plac8 induced further differentiation into proteolytic cells, resulting in massive proteolysis of pleural ECM and inward transfer of digested macromolecules (Fig. 3b, c). High resolution multi-photon images showed a reorganization of ECM occurred at pleural surfaces, consistent with ECM proteolytic disassembly, accompanied by interstitial accrual of macromolecules (Fig. 3d). Proteolytic activity was confirmed by increased Ctsb expression on mesothelial cells (Supplementary Fig. 4b). Finally, overexpression of the fibrogenic driver Mgp, induced mesothelial-to-mesenchymal transition, cell migration and α-SMA protein expression, consistent with a fibrogenic cell fate (Supplementary Fig. 4c).

Forced mesothelial differentiation results in lung fibrosis

To directly investigate the role of mesothelial cell state drivers in disease progression, we transfected AAV into the pleural space in animals, then injected NHS-FITC intrapleurally to label the ECM there, followed by Bleomycin instillment through the trachea to induce lung fibrosis (Fig. 4a). ECM labeling protocol adopted from ref. 28 was used to track ECM movement and structure in the pleural surface.

We confirmed transfection occurred exclusively on mesothelial cells, with no detectable expression in AT2 cells (pro-SPC$^-$) or macrophages (F4/80$^-$) (Fig. 5a and supplementary Fig. 5). In the AAV transfection setup control, Bleomycin-instilled lungs had decreased lung function, increased weight loss, and decreased survival rates down to 70% (Fig. 4b–d). Ashcroft scores of treated lungs, 14 days post-Bleomycin, revealed increased fibrosis with clear damage to lung structure with fibrous bands. Bleomycin induced profuse migrations of mesothelial cells from pleural lining into deep lung tissues that were α-SMA-positive (Fig. 4e). At the peak of fibrosis development, 14 days post-Bleomycin, 40% of total α-SMA-positive cells within fibrotic foci were from the pleura (Fig. 5b). This confirms the fibrogenically active mesothelial cell state contributes to lung fibrosis.

To assess the role of the metabolic cell state to fibrosis development, we transfected pleural surfaces with AAVs overexpressing the Ifi27l2a metabolic state driver. Four days post-transfection, animals were divided into two groups, one receiving intra-tracheal PBS, and another receiving Bleomycin to induce fibrosis. Remarkably, directed differentiation of pleural surfaces into metabolically active cells, with our Ifi27l2a driver, protected lungs from fibrosis. Ifi27l2a-transfected animals all survived and rapidly recovered their body weight after Bleomycin administration (Fig. 4b, c). Structurally, Ifi27l2a-transfected lung surfaces lacked fibrosis throughout the interior of the lungs, with minimal to non-existent fibrous thickening of pleural, alveolar, or bronchiolar walls and minimal α-SMA+ expressions (Fig. 4e and Fig. 5c).

Next, to assess the role of the proteolytic mesothelial cell state driver to fibrosis development, we transfected pleural lining mesothelium with AAVs overexpressing Dcn and harvested lungs 14 days post-transfection. In the absence of Bleomycin instillment, Dcn-transfected animals had less body weight, impaired lung function, and thickening and disassembly of the ECM on lung surfaces (Fig. 4b, c). Confocal microscopic observations showed pleural ECM (labeled with NHS-FITC) underwent proteolysis with larger lacunarity and porosity between fibers, accompanied by inward transfer of pleural-born ECM into deep lung tissue. Immunostaining confirmed that the proteolytic enzymes Ctsb and Mmp8 were both upregulated on mesothelial cells in response to Dcn overexpression, similarly to their upregulation in response to Bleomycin treatments (Fig. 4e and Fig. 5d).

Then, we assessed the importance of differentiation to the fibrogenic mesothelial state by transfecting pleural lining mesothelium with AAVs overexpressing the fibrogenic driver Mgp in healthy animals. Lungs harvested at 14 days post-transfection had

https://doi.org/10.1038/s41467-025-63990-2

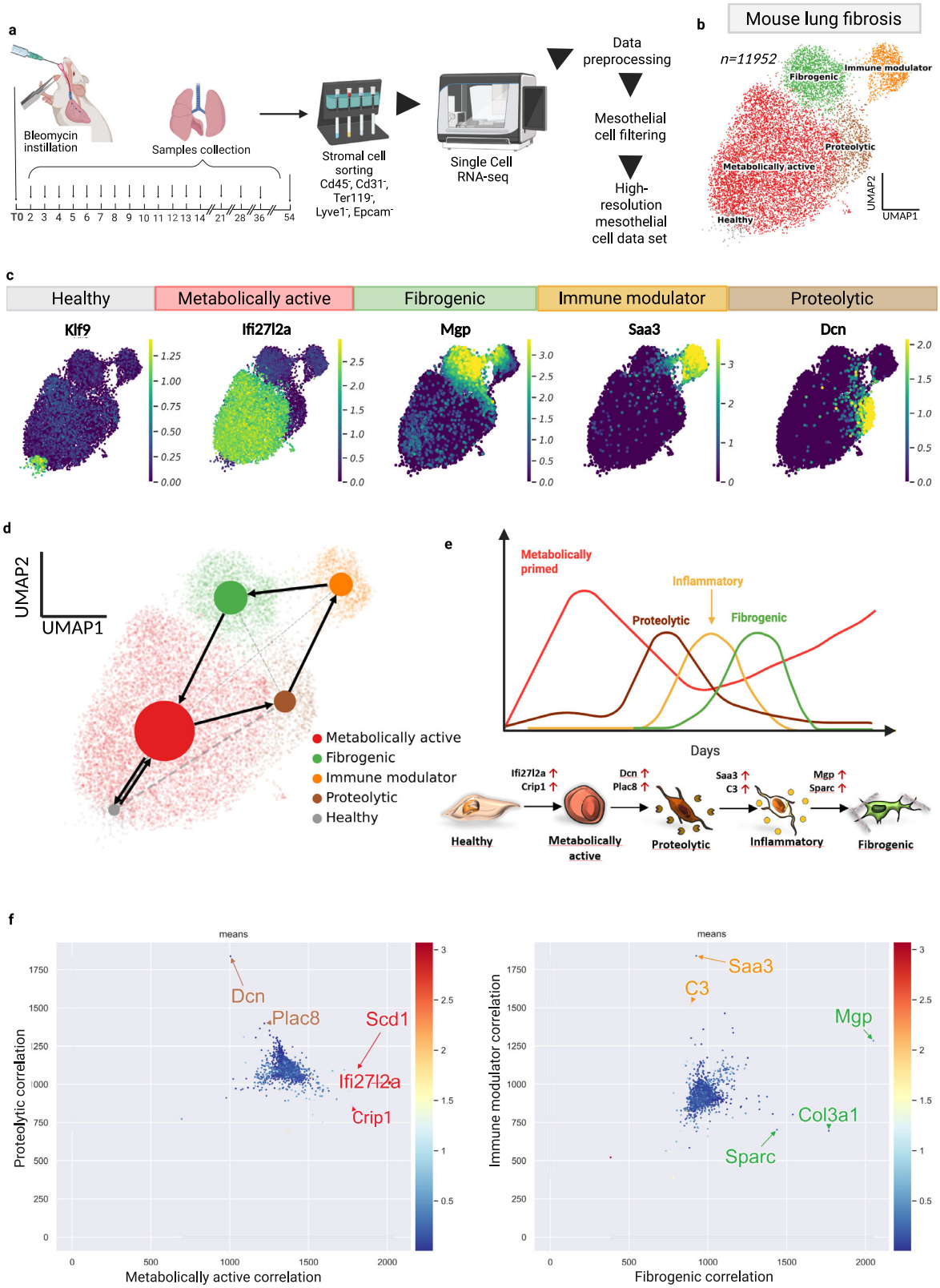

accumulation α-SMA-positive cells and fibrotic foci within deep lung tissue; they had decreased body weight and decreased survival. Mgp overexpression on pleural surfaces of these healthy lungs led to impaired lung function and increased Ashcroft scores (Fig. 4b, c). Using Ashcroft scoring, we observed that lung architectures in Dcn and Mgp overexpressing mice exhibit features resembling those of fibrotic lungs when compared to healthy controls, including pleural thickening, alveolar wall thickening, and the emergence of small fibrotic foci. Our pleural lineage-tracing combined with immunostaining confirmed that reprogramming mesothelium into fibrogenic mesothelial cells, directly induces fibrosis, expression of α-SMA within lung parenchyma and formations of fibrotic foci (Fig. 4e). To further confirm the de novo deposition of collagen by the mesothelial cells in the interstitial lung tissue we generated a Collagen1 (Col1) reporter

Fig. 2 | Time-resolved scRNA-seq data of mesothelial cells in the lung Bleomycin-induced fibrosis model. **a** Schematic of the sample preparation for the high-resolution mesothelial cell scRNA-seq dataset. Wild type mice received a single shot of Bleomycin at day 0. Lungs were harvested on the selected days (day 2 to day 54) and digested. Single cell suspensions were then sorted using Max sorting (negative gating for Cd45, Cd31, Ter119, Lyve1). Single cell suspensions were analyzed using scRNAseq. **b** UMAP of the time-scaled high-resolution mouse Bleomycin mesothelial cell dataset, color-coded for the newly identified lineages. **c** UMAP of the novel mesothelial cell lineages, highlighting the expression of the gene markers of the different clusters: Klf9 for Healthy, Ifi27l2a for metabolically active, Dcn for proteolytic, Saa3 for immune-modulator and Mgp for fibrogenic. **d** Partition-based graphic abstraction of the trajectories between the different identified populations. Upon Bleomycin installation, mesothelial cells differentiate to metabolically active cells. These metabolically active cells give rise to proteolytic cells. The proteolytic cells differentiate into immune modulator cells then into fibrogenic cells which eventually revert back to metabolically active cells. **e** Graphic predicting trajectory of interconversion of different mesothelial cell population relative abundance during Bleomycin-induced injury (x axis, day 0 to day 54). Up-regulated genes are shown for each step in the illustration underneath. **f** Gene driver plot, produced using the CellRank package, of the differentiation from metabolically active to proteolytic (right plot) and from Immune modulator to Fibrogenic. Plots highlight the most distinguishing genes corrrelating with the phenotype differentiation process. Created in BioRender. Kadri, S. (2025) https://BioRender.com/onyksnk.

AAV (Fig. 5e). Pleura mesothelial lining was transfected 4-day prior intratracheal bleomycin instillation. Confocal images shows mesothelial cells inward migration associated with the newly deposited Col1 (Fig. 5f, g). In addition, hydroxyproline measurements were performed for each group using the Enzymatic Hydroxyproline Assay (Fig. 4g), and the results were consistent with the histological measurements, providing additional validation for our findings.

Directed conversion into fibrogenic and proteolytic states with Dcn and Mgp drivers, did not lead to the protective effects seen with metabolic conversion by Ifi27l2a. In the presence of Bleo treatments, directed proteolytic and fibrogenic conversions worsened lung fibrosis, with accelerated morbidity, mortality, and more rapid weight loss. Mgp-transfected Bleomycin-treated lungs underwent pleural thickening, with accelerated ECM proteolysis and inward accrual of fibrotic foci (Supplementary Fig. 6). Ashcroft scores in these animals increased to 7, reflecting severe fibrosis phenotypes, which were absent from control Bleo experiments. Overall, these data demonstrate that mesothelium plays multiple roles in fibrosis development, and that directed pleural modulation with our drivers may reduce lung fibrosis. Ifi27l2a, Dcn and Mgp thus represent key therapeutic opportunities.

A mesothelial cell compendium across human organs

To gain a global view of all mesothelial cell states during human health, we extracted, merged, and analyzed mesothelial cells from twenty-two different human scRNA-seq datasets, representing eleven different human organs: lung, heart, liver, kidney, stomach, gut, colon, mesentery, vasculature, omentum, and adipose tissue. Human mesothelial cells clustered into nine different cell states, each with unique transcripts. As with our mouse cell types, certain human mesothelial cell types were multi-organ, whereas others were organ-specific. Shared types included pleura-visceral cells expressing TMSB10, gut-lung-mesenteric cells expressing macrophage migration inhibitory factor (MIF), Adipose-omentum expressing actin gamma 1 (ACTG1) and a universal multi-organ cell group expressing Receptor For Activated C Kinase 1 (RACK1) in gut, colon, mesenteric, stomach, lung and aorta. As in mice, human lung had the same two healthy cell types expressing PTMA and COX1, separately. Similarly, human adipose tissue had the same mesothelial types, overexpressing NALCN and ACTG1, as seen in mouse. These findings indicate mammalian conservation of mesothelial cell states and functions across organs (Fig. 6a, b).

Hierarchical clustering analysis of the human mesothelial cells across all organs revealed similarities between cells from similar organs and cavities (Fig. 6c). Human and mouse mesothelial cell groups shared homology. For example, human and mouse both have lung specific COX1+ cells. Similarly human and mouse both have visceral Tmsb10+ subsets. The human multi-organ RACK1 lineage was uniquely exclusive to human mesothelium. However they do resemble mouse liver-kidney-omentum Actg1+, mouse visceral and cardiovascular Tmsb10+, Mouse Aorta Dpt+ and mouse adipose specific Nalc+ cells (Fig. 6d), indicating a possible relationship between these more restricted cell states (Supplementary Fig. 7a, b).

In human we also found that the mesothelial cell states were disease dependent. For example, there were two different types of mesothelial cells in the healthy condition: COX1+ and PTMA+. Healthy COX1+ mesothelial cells are associated with post-translational protein modification, matrisome and ECM organization. On the other hand, pathways associated with healthy PTMA+ were the innate immune system, cytokine signaling in immune system and signaling by interleukins, suggesting a more specific role of PTMA+ cells as an immune modulator subpopulation (Fig. 6e and Supplementary Fig. 7c, d).

Moreover, we observed three types of mesothelial cells in human lung disease corresponding to the disease condition: (i) ILD-Covid mesothelial cells with markers such as MGP and Galectin 1 (LGALS1), (ii) IPF mesothelial cells with markers like IFI27L2A and CRIP1 and (iii) Smoker-Adenocarcinoma mesothelial cells with markers including Serum Amyloid A3 (SAAP3) and Aldo-Keto Reductase Family 1 Member C2 (AKR1C2). The differentially expressed genes and different functions are illustrated in Fig. 6f.

Cross-species comparison analysis using scArches demonstrated transcriptomic equivalences between the mouse and human cell types. Briefly, the model was trained on the mouse dataset to distinguish the different populations, then applied on the human dataset to map the cells onto the corresponding mouse cell types. We found that human mesothelial cells in idiopathic pulmonary fibrosis have a similar expression profile to mouse metabolically active cells with similar markers such as IFI27L2A and CRIP1 (Fig. 6g). We also found that Interstitial lung disease and Covid-19 mesothelial cells have similar expression patterns, with both mouse fibrogenic and proteolytic mesothelial cells, with markers MGP and CCDC80. The third disease population included smokers and adenocarcinoma mesothelial cells with markers such as SAA3P and AKR1C2 and this mapped to the mouse immune modulator subtype. All these data demonstrate the cross-disease conservation of mesothelial cell states.

Functional enrichment of biological terms confirmed that Healthy COX1+ cells are involved in protein secretion and golgi vesicle transport (which are related to matrisome and extracellular matrix organization) and that Healthy PTMA+ has immune modulator functions. The ILD-Covid group is functionally enriched for epithelial mesenchymal transition (EMT), with an equivalent mouse cell group. In fact, ILD-Covid cell types mapped to the fibrogenic mouse cells, which are also enriched for cell migration and mesothelial to mesenchymal transition. To confirm the markers identified for the five different human lung mesothelial cell states, we performed immunohistochemistry analysis and found that the different markers are indeed expressed in mesothelial cells in the respective populations: PTMA and KLF9 for healthy; MGP for ILD-Covid; CRIP1 for IPF and SAA3P for Smoker-Adenocarcinoma (Fig. 6h and Supplementary Fig. 7e, f).

In sum, our findings present an in-depth and comprehensive profile of mesothelial cell states and their genetic drivers, across

https://doi.org/10.1038/s41467-025-63990-2

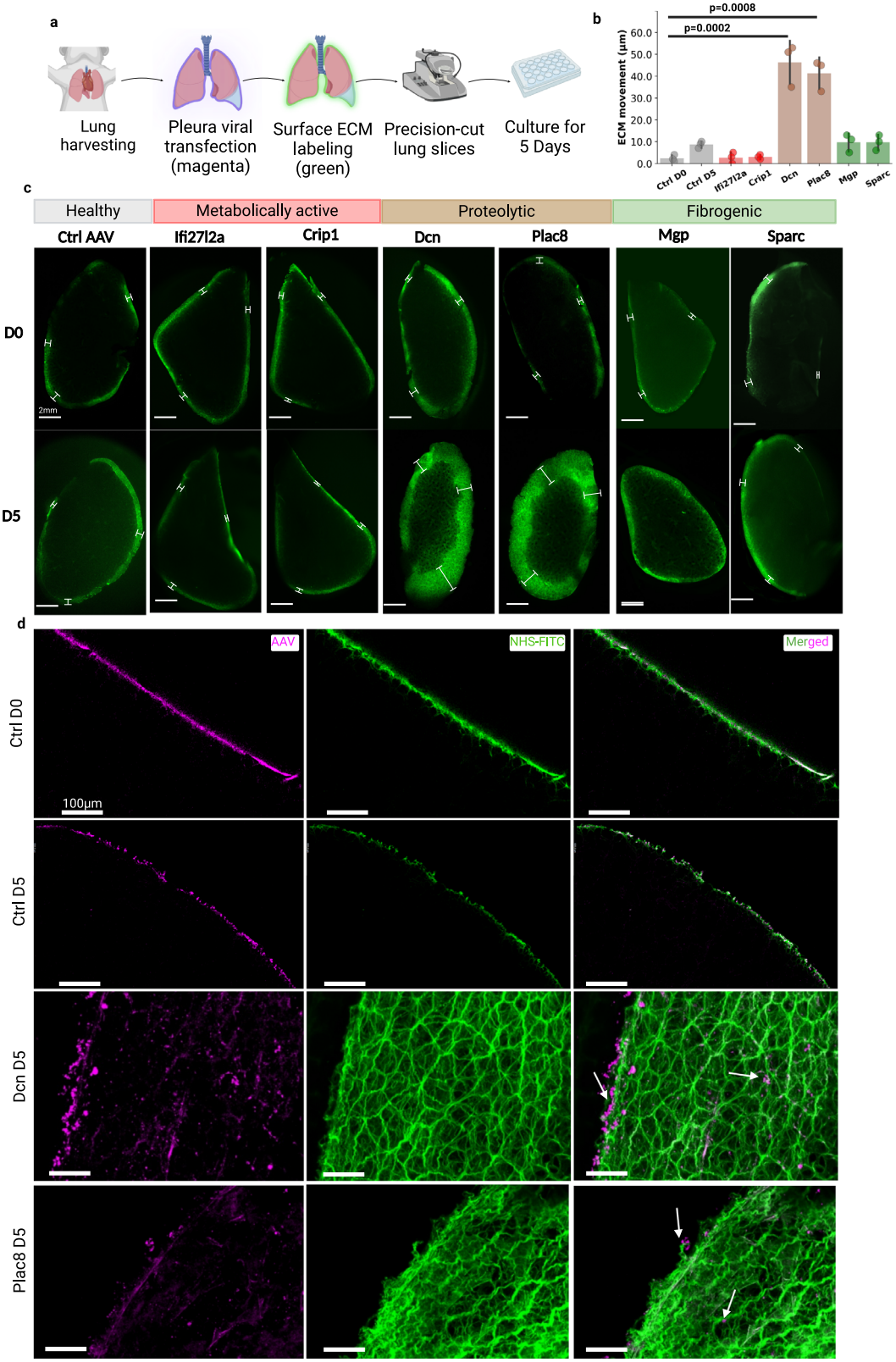

mouse and human diseases (Fig. 7). Directed reprogramming of organ surfaces opens therapeutic opportunities for the prevention and treatment of organ diseases.

Discussion

Previously, mesothelial cells were annotated into just two different states: "healthy" or "activated"[29–34]. Here we reveal, mesothelial cells transition through no less than four different cell states during fibrosis. Mesothelial cells initially differentiate to become metabolically active (i). After several days, in bleomycin-induced fibrosis, this metabolically active population gains a proteolytic phenotype (ii). The proteolytic cells then transition into an immune-modulatory phenotype (iii), before finally becoming fibrogenic (iv).

Fig. 3 | Ex vivo functional validation of the mesothelial cell populations. **a** Schematic representation of the precision cut lung slice protocol, in which mesothelial cells were transfected and ECM surface was labeled to assess ECM digestion and inward movement. The first step after lung harvesting was lung incubation with the viral particles (2 h) followed by the ECM labeling using NHS-FITC. The lung slices were cultured for 5 days. **b** Histogram of ECM movement (x axis) inside the lung slices after culture for 5 days with the overexpressed genes indicated on the y axis, colored according to the legend underneath. $N = 3$ biological replicates (C57BL/6J WT mice) and three independent experiments. A two-sided independent *T*-test was used for the comparison of two groups. Data are presented as mean values ± SEM. Source data are provided as a Source Data file. **c** Fluorescent microscopy images of lung slices, that had their surface ECM labeled at day 0, and were then transfected with the indicated AAVs: control virus, Ifi27l2a and Scd1 (markers of metabolically active), Dcn and Plac8 (markers of proteolytic), Mgp and Sparc (markers of fibrogenic). The thickness of the surface is indicated by white bars. $N = 3$ biological replicates (C57BL/6J WT mice) and three independent experiments. Scale bar is 2 mm. **d** High magnification multiphoton microscope images of the lung slices after 5 days of culture, highlighting the surface ECM (green labeling) and transfected mesothelial cells (magenta). Note the enormous increase of ECM in Dcn- and Plac8-transfected slices and the punctate expression of those proteins (white arrows in the merged image). $N = 3$ biological replicates (C57BL/6J WT mice) and three independent experiments. Scale bar is 100 μm.Created in BioRender. Kadri, S. (2025) https://BioRender.com/wburpzt.

Each cell type has a different role in the pathogenesis of lung fibrosis. According to our analysis, the initial metabolic activation, provides a gateway toward disease progression by blocking cellular differentiation. Focal adhesion, tight junctions, actin cytoskeleton and EMT are also all compromised in metabolically activated cells. By contrast, the cell cycle and cell division are upregulated.

We discovered two important genes that drive mesothelial cells toward metabolic activity: Crip1 and interferon-induced gene Ifi27l2a. Crip1 is known to be regulated by transforming growth factor-β1 (TGF-β1) and it is expressed in lung fibrosis[35]. Ifi27l2a has also been found in infected lungs[36]. Crucially we show that overexpressing Ifi27l2a protects lungs from fibrosis.

After the initial activating differentiating step, the metabolically active cells then give rise to two different pathologic cell states: proteolytic and fibrogenic. Proteolytic mesothelial cells express proteases in the extracellular domain and are responsible for the degradation of ECM macromolecules at the pleural and alveolar space. The proteolytic mesothelial cells naturally express proteases, while the fibrogenic differentiated cells express collagens. These two cell states ensure constant influx of ECM macromolecules into deep lung tissue, to further drive tissues toward fibrosis.

Once fully differentiated, the fibrogenic mesothelial cells continue to contribute to ECM movement. Indeed, the fibrogenic cells are directly attached to ECM-fragments during cell migration (Supplementary Fig. 2) and overexpressing, the fibrogenic cell differentiation gene divers, Mgp and Plac8 caused ECM displacement and fibrosis (Supplementary Fig. 3).

Current model of lung fibrosis development implicates interstitial fibroblasts. The models state that these fibroblasts are activated, by injury, to synthesize and deposit fibrotic material into lung interstitium[37]. This sequence of events it thought to be initiated by immune modulators TGF-β1, IL- β1 and PDGF.

Our findings provide a new scenario, by which material is propelled into lung tissue from pleural surfaces to contribute to fibrosis. At day 10, in the Bleomycin model, mesothelial cells differentiate from proteolytic cells to give rise to transient immune modulatory cells that express chemoattractant and complement proteins. We previously demonstrated that neutrophils direct preexisting matrix to initiate repair in damaged tissues[11]. We can now place proteolytic mesothelial cell subtype as upstream and obligatory for ECM dislodgment into injury sites to occur. These proteolytic cells can either further differentiate into fibrogenic cells, to enhance fibrosis, or they can de-differentiate back into metabolically active cells, in which case fibrosis subsides and resolves. These previously hidden cell states and their differentiation regulators in mesothelium, are a clinical handle on fibrotic disease progression that promise control of fibrotic disease across a range of clinical settings. While our single-cell analysis supports the sequential relationships of these mesothelial states, we acknowledge that some of the observed transcriptional patterns may be influenced by technical limitations associated with the method used. Despite applying rigorous quality control, we cannot fully exclude the possibility of residual technical artifacts. Future studies will be important to further validate these findings.

Methods

Animals

Wild type mouse lines (C57BL/6J), were obtained from Charles River. Animals were bred and maintained in the Helmholtz Animal Facility in accordance with EU directive 2010/63. Animals were housed in individual ventilated cages, and animal housing rooms were maintained at a constant temperature of 20–24 °C and humidity of 45–65% with a 12-h light cycle and were supplied with water and chow ad libitum. All animal experiments were reviewed and approved by the Government of Upper Bavaria and registered under the project number ROB-55.2-2532.Vet_02-19-101 and conducted under strict governmental and international guidelines. This study is compliant with all relevant ethical regulations regarding animal research.

Experimental design and animal treatment

Mice were divided randomly into two groups: (A) saline-only (PBS), or (B) bleomycin (Bleo). Lung injury and pulmonary fibrosis were induced by single-dose administration of bleomycin hydrochloride (Sigma Aldrich, Germany), which was dissolved in sterile PBS and given at 3U/kg (intratracheal instillation) bodyweight. The control group was treated with sterile PBS only. Mice were sacrificed at designated time points (days 1–14, 21, 28, 35, 56) after instillation. Treated animals were continuously under strict observation with respect to phenotypic changes, abnormal behavior and signs of body weight loss.

Human tissue

Resected lung tissue and lung explant material was obtained from the CPC-M bioArchive at the Comprehensive Pneumology Center (CPC), Munich. ILD and IPF diagnosed lung tissue ($n = 3$ each) derived from lung explant material. These tissues are obtained during lung transplantation and consist of non-resolving end-stage fibrotic lung disease and diagnosed as IPF. Healthy control tissue ($n = 3$) was derived from tumor resection in no other chronic lung disease patients. Smoker lung tissue ($n = 3$) was derived from tumor resection from smoker patients with no other chronic lung disease.

Labeling of ECM on organ surfaces

Succinimidyl esters (N-Hydroxysuccinimide (NHS)-esters; 1308 Thermo Fisher) were diluted in DMSO to a concentration of 25 mg/ml and stored at −80 °C. To achieve ectopic labeling of matrix, we generated a labeling solution by mixing NHS-ester solution 1:1 with 100 mM pH 9.0 sodium bicarbonate buffer. For in-vivo experiments, we generated a labeling solution by mixing 5 μl Succinimidyl esters (NHS-esters; Thermo Fisher) from stock solution (25 mg/ml) with 5 μl of 100 mM pH 9.0 sodium bicarbonate buffer. This was combined with 40 μl PBS to a total volume of 50 μl. Labeling solution was applied intra pleurally under isoflurane anesthesia with a 30G cannula. For precision-cut lung slices ECM labeling, sterile Whatman filter papers (Sigma Aldrich) were soaked in NHS-labeling solution and placed on

https://doi.org/10.1038/s41467-025-63990-2

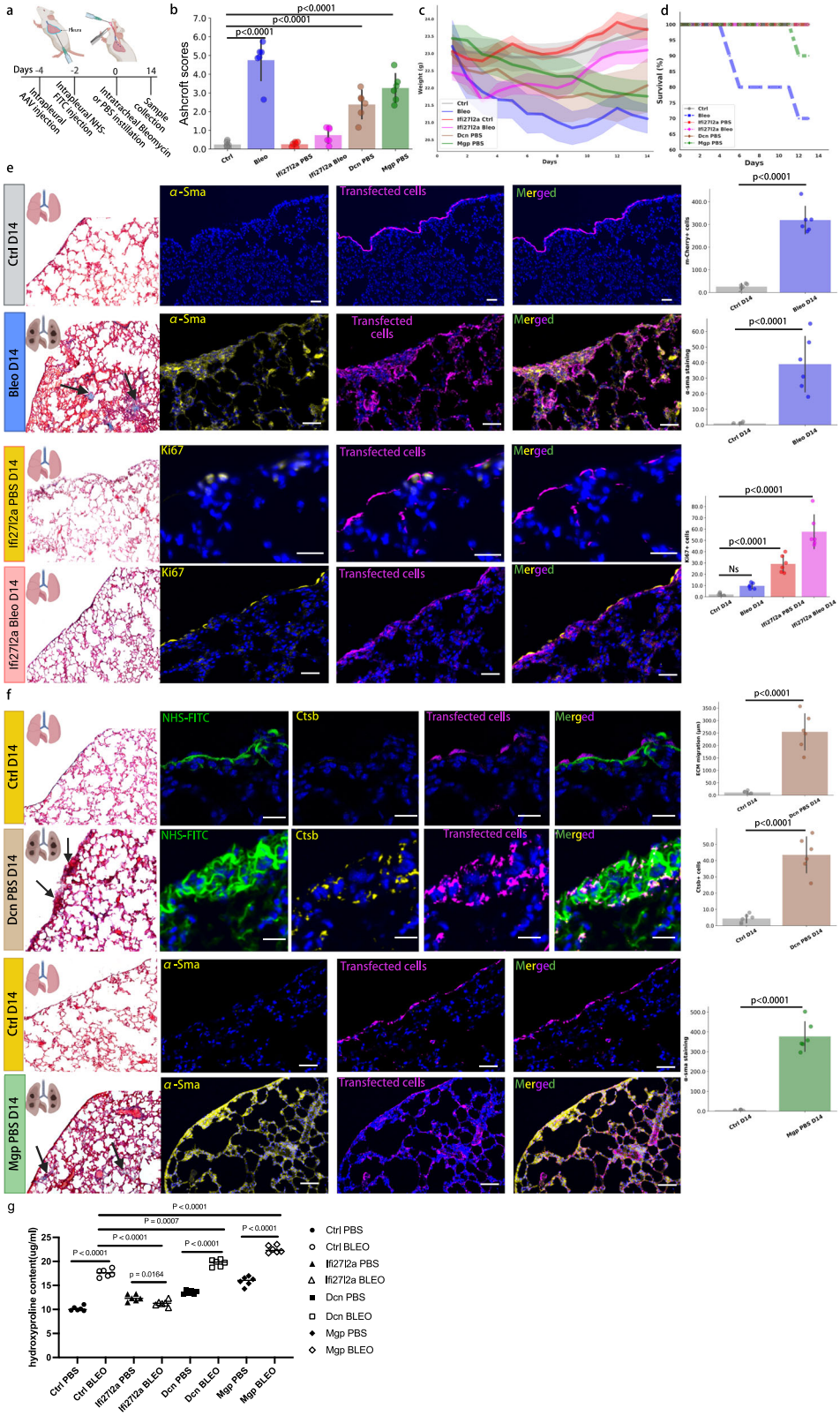

the whole lung lobe. After 1 min, the labeling Whatman filter paper was removed. Tissue was washed with PBS 3 time to remove excess of labeling.

AAV production

Production and purification of AAV preparations for AAVCNA35m-Cherry was performed according to the AAVpro Purification Kit Maxi (Takara Bio) protocol. In brief, five T225-flasks were triple-transfected with the following three plasmids: (i) plasmid pHelper from the AAVpro Helper Free System kit (Takara Bio), (ii) the plasmid pAAV2/8RGD containing coding sequences of the AAV2-derived rep proteins and the modified AAV8 capsid proteins and (iii) the pAAV-Cp-SV40pA derivative containing the AAV genome with the respective transgene. At 96 h post-transfection, cells were collected and AAV vector particles were

Fig. 4 | Metabolically active mesothelial cell differentiation genes drive fibrosis. **a** Treatment scheme for candidate gene overexpression in lung mesothelium. **b** Ashcroft scores by using the trichrome staining of the lung sections in the different conditions: Control PBS (Ctrl); Control AAV Bleomycin (Bleo); Ifi27l2a AAV PBS (Ifi27l2a PBS); Ifi27l2a AAV Bleomycin (Ifi27l2a Bleo); Dcn AAV PBS (Dcn PBS) and Mgp AAV PBS (Mgp PBS). $N = 6$ biological replicates (C57BL/6J WT mice) and three independent experiments. A two-sided independent *T*-test was used for the comparison of two groups. Data are presented as mean values ± SEM. Source data are provided as a Source Data file. **c** Daily body weight lost in the different groups. Data are presented as mean values ± SEM. Source data are provided as a Source Data file. **d** Experimental group survival rates. Source data are provided as a Source Data file. **e** Lung function impairment in the different conditions: Trichrome staining images of the control PBS, control bleomycin, Ifi27l2a PBS, Ifi27l2a bleomycin (from up to bottom) with arrows highlighting fibrotic clots (Ctrl and Bleo). On the right: confocal images of the lung stained with different staining: α-sma, Ki67 (both yellow) and mesothelial transfected cells (magenta). On the right-hand side, the quantification of the different immunostaining. $N = 6$ biological replicates (C57BL/6J WT mice) and three independent experiments. A two-sided independent *T*-test was used for the comparison of two groups. Data are presented as mean values ± SEM. Scale bar is 20 μm. Source data are provided as a Source Data file. **f** Lung function impairment in the different conditions: Trichrome staining images of the control PBS, Dcn PBS, control PBS, Mgp PBS (from up to bottom) with arrows highlighting fibrotic clots (Ctrl and Bleo). On the right: confocal images of the lung stained with different staining: extracellular matrix (NHS-FITC), Ctsb, α-sma (both yellow) and mesothelial transfected cells (magenta). On the right-hand side, the quantification of the different immunostaining. $N = 6$ biological replicates (C57BL/6J WT mice) and three independent experiments. A two-sided independent *T*-test was used for the comparison of two groups. Data are presented as mean values ± SEM. Scale bar is 20 μm. **g** Hydroxyproline measurements were performed for each group using the Enzymatic Hydroxyproline Assay. $N = 6$ biological replicates (C57BL/6J WT mice) and three independent experiments. A two-sided independent *T*-test was used for the comparison of two groups. Created in BioRender. Kadri, S. (2025) https://BioRender.com/s4fbbop.

released by breaking up the cells through three freeze–thaw cycles. Genomic DNA was digested with Cryonase cold-active nuclease, and AAV vector particles were separated from cell debris by filtration (0.45-μm filter). Finally, AAV particles were separated from low molecular weight contaminants by using 100-kDa size-exclusion columns. Titers of final AAV preparations were determined by qPCR utilizing the AAVpro Titration Kit (qPCR) V2 (Takara Bio). Local AAV labeling was performed using sterile Whatman filter papers, as described above for NHS ex-vivo surface labeling.

Precision-cut lung slicing and in vitro culture

Precision-cut lung slices (PCLS) were obtained from mouse lungs according to the protocol described in ref. 19, with some modifications. Adult C57BL/6 mice (10 weeks old) were humanely killed by intraperitoneal injection of pentobarbital. The anterior chest wall was excised and trachea was carefully exposed. A tiny opening was made in the anterior wall of the trachea just below the cricoid cartilage. A rigid metallic cannula (21G) was carefully inserted through the trachea up to a millimeter above the bifurcation of the principal bronchi and fixed in place by suture. After cannulation, the lungs were inflated with 37 °C 1.5% low-melting-point agarose (Sigma; Cat. No. A9414) prepared with 1× serum-free DMEM (SF-DMEM) (Life Technologies; Cat. No. 31966-021). Agarose was injected to inflate both lungs keeping them in situ within the chest cavity at volume that enabled lungs to be fully inflated without hyper- or sub-optimal inflation (1 ml agarose). After inflation, agarose was solidified by applying ice to the chest cavity for 1 min. Subsequently, the lungs were excised from the body along with heart and trachea and immersed in ice-cold SF-DMEM and kept on ice until slicing. Left lung lobes were isolated and cut transversely at 300 μm using a vibratome (Zeiss Hyrax V50) in ice-cold SF-DMEM buffer. Slices were obtained from the middle 2/3rds of the lobe to ensure similar sized slices and placed in a 24-well plate in ice-cold SF-DMEM for all experiments. PCLS were then incubated at 37 °C for 2 h and washed twice with warm SF-DMEM to remove excess agarose from the tissue. PCLS were cultured for up to 120 h in presence of 5% CO2 and 95% air at 37 °C in M199 media (Life Technologies; Cat. No. 11150059) supplemented with Insulin/transferrin/selenium (Life Technologies; Cat. No. 41400045), vitamin C (Cat. No. A4403), vitamin A (Cat. No. R2625), hydrocortisone (Cat. No. H4001), 1% penicillin–streptomycin (All from Sigma) as described previously (10.1165/rcmb.2013-0056OC) and media was changed every 2nd day. After incubation PCLS were fixed with 4% paraformaldehyde for 2 h at 4 °C and prepared for imaging and immunostaining.

Tissue preparation

Upon organ excision, organs were fixed overnight at 4 °C in 4% paraformaldehyde. The next day, fixed tissues were washed three times in Dulbecco's phosphate buffered saline (DPBS, GIBCO, no. 14190-094), and frozen in optimal cutting temperature compound (Sakura, no. 4583) and stored at −20 °C. Fixed and embedded tissues were embedded and cut with a Microm HM 525 (Thermo Scientific) by the standard protocol. For antigen retrieval sections were incubated in ice-cold acetone for 5 min at 4 °C and then washed with PBS. Sections were either used for Masson's Trichrome staining or for immunohistochemistry.

For Immunohistochemistry, slices were blocked for non-specific binding with 5% non-immune secondary antibody host serum (UCSF Cell Culture Facility) in PBS for 60 min at room temperature, and then incubated with primary antibody in blocking solution overnight at 4 °C. The next day, following 3 times PBS washing, sections were incubated in PBS with fluorescent secondary antibody, for 120 min at room temperature. Finally, sections were washed three times with PBS and mounted with Fluoromount- with DAPI (Life Technologies, 00-4959-52), and stored at 4 °C in the dark. Masson's trichrome staining was performed using a commercial kit (Sigma Aldrich HT15) following manufacturer's recommendations. Fibrosis severity was assessed using the Ashcroft scoring system. For each lung lobe, three representative non-overlapping regions were selected and scored by two trained laboratory personnel who were blinded to the experimental groups. The scores from the selected regions were averaged for each lobe to obtain a fibrosis assessment. To ensure the consistency of the Ashcroft scoring, the same regions were analyzed across adjacent sections, and inter-scorer agreement was evaluated statistically to confirm the reliability of the scores. To quantify collagen content, a hydroxyproline assay was performed using a commercially available kit (Hydroxyprolin Assay-Kit, ab222941, abcam). Hydroxyproline content was assessed from whole lung tissue. Every 10 mg of lung tissue was homogenized in 100 µL distilled water using an ultrasonic probe homogenizer. A 100 µL aliquot of the homogenate was transferred to a pressure-tight polypropylene vial, followed by the addition of 100 µL of 10 N NaOH. Samples were hydrolyzed at 120 °C for 1 h, cooled on ice, and neutralized with 100 µL of 10 N HCl. After centrifugation at 10,000 × *g* for 5 min, the supernatant was collected and used for hydroxyproline quantification. The hydrolyzed samples were evaporated at 65 °C and subjected to oxidation and colorimetric detection according to the manufacturer's protocol. Absorbance was measured at 560 nm using a microplate reader, and hydroxyproline concentration was calculated based on a standard curve.

Primary antibodies were used: α-sma (Abcam ab21027 1:200), Ki67 (Abcam ab16667 1:200), Cathepsin B (Elabscience E-AB-10208.120 1:100), Crip1 (Sigma SAB2105782 1:500), Dcn (Abcam ab277636 1:200), Saa3 (Biozol GTX03433 1:250), Mgp (Biomol ARG58960.100 1:200), Ptma (Abcam ab247074 1:200), Cox1 (Sigma SAB2500266 1:200), Gpm6a (Bio-techne NBP1-68861 1:500), EMT Marker antibody

https://doi.org/10.1038/s41467-025-63990-2

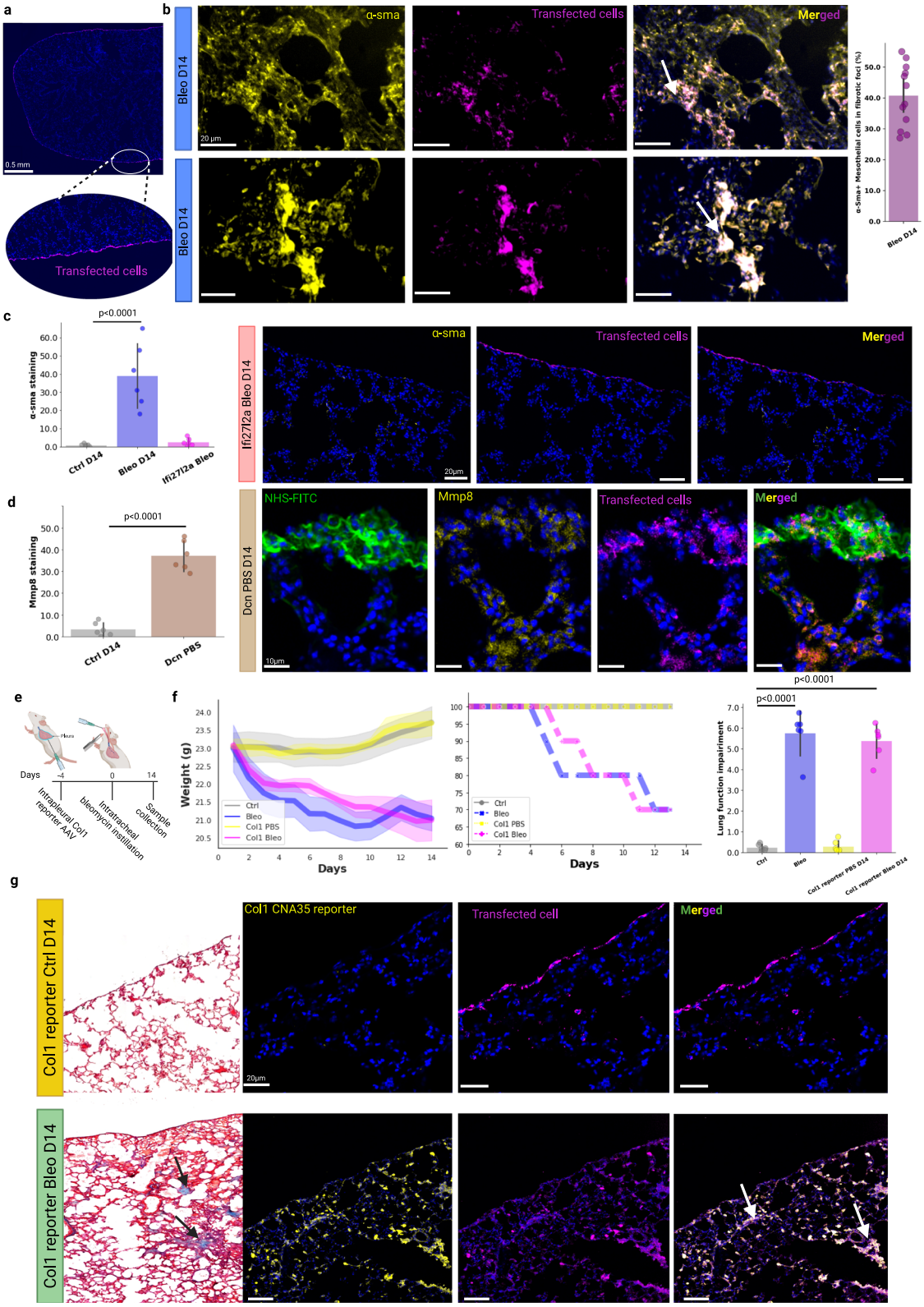

panel (Biomol ARG30320 1:500), MMP8 (Elabscience E-AB-60525 1:200), Ifi27l2 (Biozol ASB-OACA06337 1:200), F4/80(eBioscience 14-4801-85 1:100) and ProSPC(Abcam ab90716 1:100).

Alexa-Fluor-488-, Alexa-Fluor-568- or Alexa-Fluor-647-conjugated antibodies (1:500, Life Technologies) against suitable species were used as secondary antibodies. Trichrome staining was performed according to the manufacturer's protocol (HT15-1KT-Sigma).

Microscopy

Masson's trichrome stained sections were imaged under a M205 FCA Stereomicroscope (Leica) and ZEISS AxioImager Z2m (Carl Zeiss). For precision-cut lung slice imaging, fixed samples were embedded in 35-mm glass-bottom dishes (Ibidi) with low-melting-point agarose (Biozym) and left to solidify for 30 min. Imaging was performed with a THUNDER Imager Model Organism (Leica) or Leica SP8 multiphoton

Fig. 5 | Immunostaining of the different markers identified in the high resolution lung fibrosis mesothelial cell dataset. a Immunostaining showing the AAV control specificity to the mesothelial cells. $N = 6$ biological replicates (C57BL/6J WT mice) and three independent experiments. Scale bar is 0.5 mm. **b** Immunostaining of α-sma of Bleomycin ctrl AAV group. Tile imaging was used to capture the lungs and performed measurements on fibrotic foci across at least 12 different regions of the affected lungs. $N = 12$ biological replicates (C57BL/6J WT mice) and three independent experiments. Data are presented as mean values ± SEM. Scale bar is 20 μm. Source data are provided as a Source Data file. **c** Immunostaining of α-sma in Ifi27l2a bleo day 14 group. $N = 6$ biological replicates (C57BL/6J WT mice) and three independent experiments. A two-sided independent *T*-test was used for the comparison of two groups. Data are presented as mean values ± SEM. Scale bar is 20 μm. Source data are provided as a Source Data file. **d** Immunostaining of Mmp8 in Dcn PBS day 14 group. $N = 6$ biological replicates (C57BL/6J WT mice) and three independent experiments. A two-sided independent *T*-test was used for the comparison of two groups. Data are presented as mean values ± SEM. Scale bar is 10 μm. Source data are provided as a Source Data file. **e** Experimental design of the collagen reporter AAV approach: AAV with col1 reporter was injected intrapleurally 4 day before the bleomycin instillation. At day 0 the bleomycin was administrated intratracheal and lungs were harvested 14 day after that. **f** Weight loss, survival curve and lung function of the different groups in the Col1 reporter experiment (from right to left). $N = 6$ biological replicates (C57BL/6J WT mice) and three independent experiments. A two-sided independent *T*-test was used for the comparison of two groups. Data are presented as mean values ± SEM. Source data are provided as a Source Data file. **g** Panel of trichrome staining and immunostaining of the Col1 reporter and the mesothelial cells. $N = 6$ biological replicates (C57BL/6J WT mice) and three independent experiments. Scale bar is 20 μm.Created in BioRender. Kadri, S. (2025) https://BioRender.com/p5gpax6.

microscope. Two- and three-dimensional data were processed with Imaris 9.1.0 (Bitplane) and ImageJ (1.52i). Contrast and brightness were adjusted for better visibility. The acquired fluorescent z-stacks were analyzed in Imaris 9.3 software (Bitplane), ECM movement, cell number, area and immunolabeling quantifications were analyzed using imageJ.

Mouse and human scRNA-seq atlas generation and meta-analysis

In order to comprehensively analyze the mesothelial cells function and relatedness across different organs we generated a steady-state mesothelial cell atlas composed of 32 datasets[38–68]. Similarly, to assess differential response and differentiation of mouse mesothelial cells across different tissue during diseases[46,55–57,59,61,69–78], we established a perturbed-state mesothelial atlas composed of 22 datasets. Furthermore, we established a healthy human mesothelial cell atlas using 23 datasets[78–94]. For the human lung mesothelial cell atlas we used 6 datasets of healthy lung that were included in the previous atlas to which we added 10 disease lung datasets[78–85,95–97] including IPF, ILD, Smoker, Adenocarcinoma and Covid-19. All Mesothelial atlases were generated and then analyzed using the following steps: (1) Processing and filtering and extracting individual mesothelial scRNA-seq datasets; (2) Dataset integration and batch removal for the four atlases; (3) Clustering and annotation of steady- and perturbed-state mesothelial atlases; and (4) Hiearchical clustering and cross species analysis. The aforementioned steps are described in detail in the following sections.

(1) Processing and filtering and extracting individual mesothelial scRNA-seq datasets: Single cell transcriptomics datasets were used to generate four different atlases of mesothelial cells: (i) steady-state mouse mesothelial cell atlas; (ii) disease-state mouse mesothelial cell atlas; (iii) steady-state human mesothelial cell atlas and (iv) human lung mesothelial cell atlas. Single cell transcriptomics datasets, generated using 10X Genomics and available as processed CellRanger files, were collected from public repositories (Supplementary Tables 1–4). For public datasets where processed files were not made available, we analyzed raw data using "cellranger count" (CellRanger 2.1.0, 10X Genomics) based on mouse reference genome GRCm38 or human GRCh38.p14 (for the human atlases). Pre-processed files were analyzed using phyton toolkit Scanpy (v1.9.0). Each raw dataset that we processed we filtered low quality cells (using scanpy.pp.filter_cell function) with <200 measured genes and a high percentage of mitochondrial contamination (>~5). After filtering low quality cells, raw data were saved to be used for the batch effect removal. After that files were processed according to the developers recommendations. The dimensional reduction method used was the UMAP algorithm. Cells were them clustered using leiden or Louvain with variable resolutions to match the author clustering and used markers. Mesothelial cells clusters were identified using the markers Msln, Wt1, Pdpn, Procr. Simmilarly, cell clusters marked by the canonical marker gene for immune cells Ptprc (Cd45), epithelial cells Epcam), endothelial cells (Cd31) and were discarded. Raw data was then recovered and all individual datasets were then used for integration to create the different atlases: a steady-state mesothelial atlas comprising data from healthy tissues in mouse and human each; a perturbed-state mesothelial atlas comprising data from diseased and inflamed tissues in mouse and a human lung mesothelial cell atlas containing steady and perturbed states.

(2) Dataset integration and batch removal for the four atlases: Before dataset integration, mesothelial cell datasets were converted into SingleCellExperiment using Seurat[98] (v4.3.0) in R (v4.2.3). Data were then merged and batch effect was removed using BatchBench package[25]. Output file we imported were converted to h5ad using Zellkonverter (v1.12.0) and imported to Scanpy. The mouse mesothelial-specific atlases included steady- and perturbed-state atlases comprising 32,134 and 5601 cells, respectively. The human steady-state atlas included 16107 cells, whether the human lung steady and perturbed-states included 5802 cells.

(3) Clustering and annotation of steady- and perturbed-state mesothelial atlases: Atlas files were processed according to developers recommendation and we used UMAP algorithm for the dimensional reduction. The clustering was performed using Leiden with variable resolution (between 0.2 and 0.5) to ensure the less possible shared markers between clusters. Differential gene expression was computed using the Scanpy function tl.rank_genes_groups using a Wilcoxon rank sum test.

(4) Hierarchical clustering and cross species analysis: Hierarchical clustering was computed for the different origin tissues using the principle components with the function tl.dendrogram within the Scanpy toolkit. The cross species analysis was performed using the scArches[99] tool. The reference dataset used was the mouse atlases. We trained the models on mouse steady-state for the human steady-state atlas and on mouse lung high resolution bleomycin dataset for the human lung mesothelial atlas. After training the model on the reference datasets, node weights were transferred to a new model. Human datasets were then tested and cells were annotated according to the respective reference dataset.

Stromal cell enrichment for scRNAseq

Three lungs per time point were pooled for each sequencing run. Lungs were subsequently minced with fine scissors into small pieces (approximately 1 mm^2). The resulting fragments were further processed by enzymatic digestion in 5 mL enzyme mix consisting of dispase (50 caseinolytic units/ml), collagenase (2 mg/ml), and DNase (30 μg/ml), for 30 min at 37 °C under constant agitation (180 rpm). Enzyme activity was inhibited by adding 5 ml of PBS supplemented with 10% FBS. Dissociated cells in suspension were passed through a 70-μm strainer and centrifuged at 500 × *g* for 5 min at 4 °C. Red blood cell lysis (Thermo Fisher; 00-4333-57) was performed for 2 min and

https://doi.org/10.1038/s41467-025-63990-2

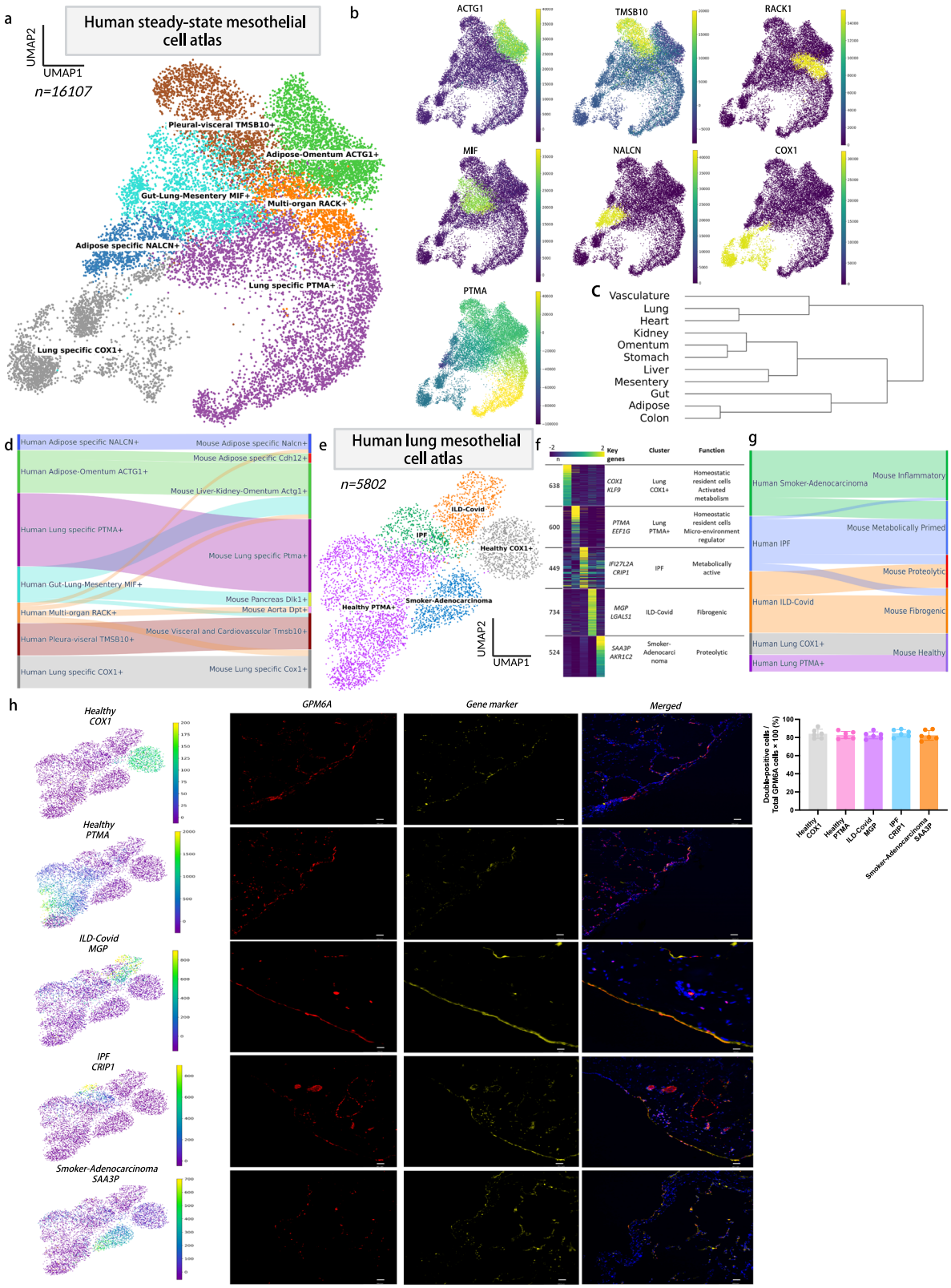

then stopped with 10% FBS in PBS. The resulted single cell suspension was filtered and incubated at 4 °C for 30 min with conjugated primary antibodies (dilution 1:200) against specific cell markers of unwanted cell type lineages. Antibodies used: APC-anti-CD31 (eBioscience 17-0311-82), eFluor660-anti-Lyve1 (eBioscience 50-0443-82), APC-anti-Ter119 (Biolegend bld-116212), Alexa Fluor 647-anti-Epcam (Biozol BLD-118212) and APC-anti-CD45 (Biolegend Bld-103112). Cells were then washed and incubated at 4 °C for 20 min with suitable magnetic beads against the conjugated fluorophores and dead cell markers (Dead Cell removal kit, Miltenyi 130-090-101). Microbeads used: Anti-Cy5/AlexaFluor647 (Miltenyi 130-090-855) and anti-APC (Miltenyi 130-091-395). Cells were separated using OctoMACS and MS columns (Myltenyi) according to manufacturer's guidelines. Negative selection was then washed, counted, and diluted at 100 cells per microliter in

Fig. 6 | Steady and disease-state human mesothelial cell atlases. a UMAP embedding of human mesothelial single cells in the steady-state atlas. Nine clusters identified through graph-based clustering are indicated by color. **b** UMAP highlighting the expression levels of the different identified markers for each cluster. **c** Hierarchical clustering of the different mesothelial cells, depending on the tissue of origin, showing the cellular progenitors of the mesothelial cells in different tissues. **d** Cross-species analysis of the corresponding identified human and mouse mesothelial cell clusters in health. **e** UMAP of the identified human lung mesothelial cells in health and disease, color coded for the annotation of the healthy state (COX1+ and PTMA+) and disease (IPF, ILD-Covid and Smoker-Adenocarcinoma). **f** Heat maps of the relative average expression of the most highly enriched genes for each cluster in disease-state human lung mesothelial atlas (log(fold change) of one cluster versus all others. **g** Riverplot comparing the identified human lung clusters to the mouse newly identified clusters using scArches. **h** UMAPs and immunostainings of the different human mesothelial healthy and disease markers co-labeled with the mesothelial marker Gpm6a as indicated. On the right-hand side, the quantification of the different immunostaining. $N = 6$ biological replicates and three independent experiments. Data are presented as mean values ± SEM. Scale bar is 200 μm. Source data are provided as a Source Data file.

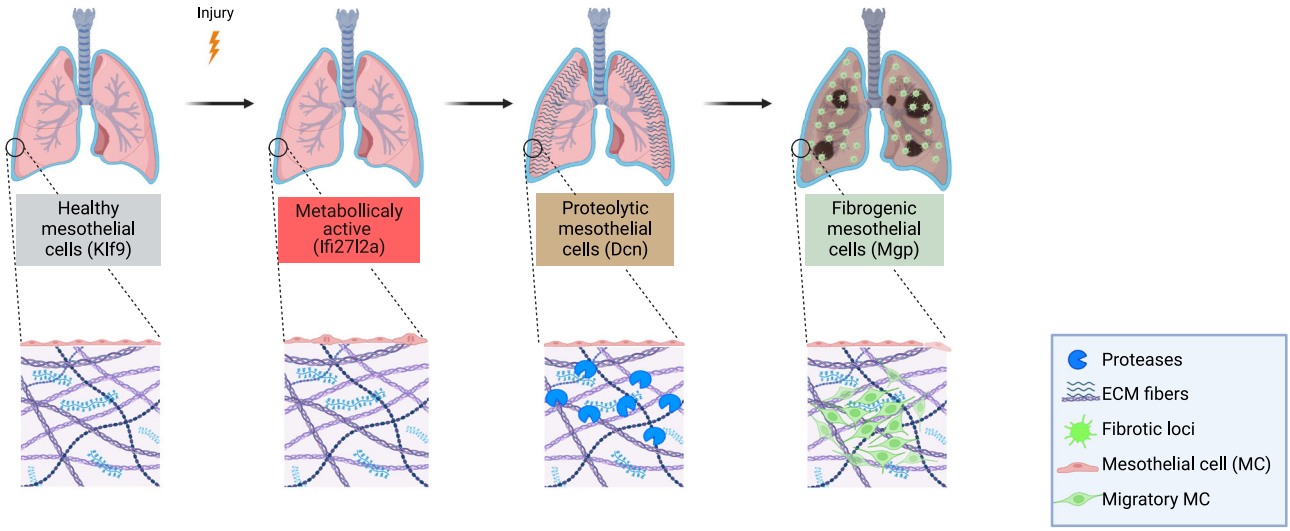

Fig. 7 | Upon lung injury mesothelial cells are activated into metabolically active mesothelial cells. Upon injury, healthy mesothelial cells are activated with various upregulated metabolic processes and more active cell division. This population named "metabolically active" is characterized by the overexpression of Ifi27l2a, Crip1 and Scd1. The metabolically active state is the first stage of mesothelial cell differentiation upon injury that then gives rise to two other cell subtypes involved in the development of lung fibrosis. (i) First there are "proteolytic cells", which overexpress proteases and are involved in the degradation of existing ECM. (ii) The second cell type are fibrogenic, with an active mesothelial to mesenchymal transition, de novo ECM deposition, and a tightened cell-ECM interaction, increased glycolytic cell decoration and immune cell invasion. Created in BioRender. Kadri, S. (2025) https://BioRender.com/k2y5xb4.

PBS with 0.04 % BSA and 300 U/ml of RNase inhibitor (RiboLock LIFE technologies eo0382). Only samples with >90 % living cells were used for Dropseq separation.

Single cell RNA-sequencing using Dropseq

Stromal-enriched cell suspensions were separated using the Drop-seq80 microfluidic-based method following the McCaroll lab protocol with a few adaptations. Briefly, using a microfluidic PDMS device (Nanoshift), cells were encapsulated in droplets with barcoded beads (120/µl, ChemGenes Corporation, Wilmington, MA) at a rate of 4000 µl/hr. Droplet emulsions were collected for 15 min/each prior to droplet breakage with perfluoro-octanol (Sigma-Aldrich). After breakage, beads were harvested, and the hybridized mRNA transcripts were reverse transcribed (Maxima RT, Thermo Fisher). Unused primers were removed by the addition of exonuclease I (New England Biolabs). Beads were then washed, counted, and aliquoted for pre-amplification (2000 beads/reaction, equals ~100 cells/reaction) with 12 PCR cycles (with the recommended settings). PCR products were pooled and purified twice by 0.6x clean-up beads (CleanNA). Prior to tagmentation, cDNA samples were loaded on a DNA High Sensitivity Chip on the 2100 Bioanalyzer (Agilent) to ensure transcript integrity, purity, and amount. For each sample, 1 ng of pre-amplified cDNA, from an estimated 1000 cells, was tagmented by Nextera XT (Illumina) with a custom P5 primer (Integrated DNA Technologies). Single cell libraries were sequenced in a 100 bp paired-end run on an Illumina HiSeq4000 using 0.2 nM denatured sample and 5% PhiX spike-in. For priming of the 1st read, 0.5 µM Read1CustSeqB (primer sequence: 5′-gcctgtccgcggaagcagtggtatcaacgcagagtac-3′) was used.STAR (version 2.5.2a) was used for mapping the reads and to align them to the mm10 genome reference (provided by Drop-seq group, GSE63269) that was tailored to include the eGFP cDNA transcript.

Analysis of the high-resolution mesothelial data set

The computational analysis of the high-resolution mesothelial cell dataset was performed using the different steps previously mentioned and in accordance to the developers recommendation of Scanpy toolkit. Mesothelial cells were selected by eliminating cells with epithelial (Epcam) endothelial (CD31), immune (Cd45) and fibroblast (Pdgfra) markers. To filter the data further, the cells were clustered and clusters expressing non-epithelial markers were excluded from the data set. Ambient RNA analysis was performed using SoupX (Version 1.6.0)[100], and doublet detection was conducted with DoubletDetection (Version 4.0)[101]. Leiden clustering was used with the high possible resolution which maintained the healthy mesothelial cells in one cluster (resolution 0.8). Trajectories were inferred by partition-based graph abstraction with RNA velocity-directed edges using the scvelo toolkit[102]. "Dynamic modeling" was used under standard settings to calculate velocities. Cells were arranged under the inferred trajectory using "velocity pseudotime" function rooting the trajectory origin in healthy mesothelial cells (day 0).

For the gene ontologies and pathway analyses we used the toolkits GSEApy[103] and decoupleR[104] implementation of AUCell[105]. For

pathway analysis we used the Reactome[106] (Version 86) and for the biological processes we used the updated version 2023-07-27[107]. For the gene drivers analysis we used the toolkit CellRank[26] to estimate fate probabilities and driver genes.

Statistics

Data were analyzed in Prism 7.0.0 (GraphPad). Statistical tests were performed as indicated in the figure legends, and *n* values are also provided. All error bars represent mean ± s.d. Mice and tissues were randomly assigned to treatment groups where applicable. No data were excluded. Data were presumed to be normally distributed. Statistical significance was defined as $P < 0.05$, for reasons of space and visibility, the individual *P* values less than 0.0001 were just mentioned as $P < 0.0001$.

Reporting summary

Further information on research design is available in the Nature Portfolio Reporting Summary linked to this article.

Data availability

The data generated in this study have been deposited at Zenodo https://zenodo.org/records/17013540. Source data are provided with this paper.

Code availability

The code generated in this study have been deposited at Zenodo https://zenodo.org/records/17013540.

References

1. Kawanishi, K. Diverse properties of the mesothelial cells in health and disease. *Pleura Peritoneum* **1**, 79–89 (2016).
2. Wang, N. S. The regional difference of pleural mesothelial cells in rabbits. *Am. Rev. Respir. Dis.* **110**, 623–633 (1974).
3. Mutsaers, S. E. & Wilkosz, S. Structure and function of mesothelial cells. *Cancer Treat. Res.* **134**, 1–19 (2007).
4. Rinkevich, Y. et al. Identification and prospective isolation of a mesothelial precursor lineage giving rise to smooth muscle cells and fibroblasts for mammalian internal organs, and their vasculature. *Nat. Cell Biol.* **14**, 1251–1260 (2012).
5. Mutsaers, S. E., Prêle, C. M.-A., Pengelly, S. & Herrick, S. E. Mesothelial cells and peritoneal homeostasis. *Fertil. Steril.* **106**, 1018–1024 (2016).
6. Soliman, F., Ye, L., Jiang, W. & Hargest, R. Targeting hyaluronic acid and peritoneal dissemination in colorectal cancer. *Clin. Colorectal Cancer* **21**, e126–e134 (2022).
7. Mutsaers, S. E., Pixley, F. J., Prêle, C. M. & Hoyne, G. F. Mesothelial cells regulate immune responses in health and disease: role for immunotherapy in malignant mesothelioma. *Curr. Opin. Immunol.* **64**, 88–109 (2020).
8. Zindel, J. et al. Primordial GATA6 macrophages function as extravascular platelets in sterile injury. *Science* **371**, eabe0595 (2021).
9. Neupane, A. S. et al. Patrolling alveolar macrophages conceal bacteria from the immune system to maintain homeostasis. *Cell* **183**, 110–125.e11 (2020).
10. Buechler, M. B. et al. A stromal niche defined by expression of the transcription factor WT1 mediates programming and homeostasis of cavity-resident macrophages. *Immunity* **51**, 119–130.e5 (2019).
11. Fischer, A. et al. Neutrophils direct preexisting matrix to initiate repair in damaged tissues. *Nat. Immunol.* **23**, 518–531 (2022).
12. Yung, S. & Chan, T. M. Pathophysiological changes to the peritoneal membrane during PD-related peritonitis: the role of mesothelial cells. *Mediat. Inflamm.* **2012**, 484167 (2012).
13. Yung, S. & Chan, T. M. Intrinsic cells: mesothelial cells—central players in regulating inflammation and resolution. *Perit. Dial. Int.* **29**, S21–S27 (2009).
14. Xiao, L., Sun, L., Liu, F.-Y., Peng, Y.-M. & Duan, S.-B. Connective tissue growth factor knockdown attenuated matrix protein production and vascular endothelial growth factor expression induced by transforming growth factor-beta1 in cultured human peritoneal mesothelial cells. *Ther. Apher. Dial.* **14**, 27–34 (2010).
15. Cao, Y. et al. Identification of enhancer regulatory elements that direct epicardial gene expression during zebrafish heart regeneration. *Dev. Camb. Engl.* **149**, dev200133 (2022).
16. Sun, J. et al. hapln1 defines an epicardial cell subpopulation required for cardiomyocyte expansion during heart morphogenesis and regeneration. *Circulation* **146**, 48–63 (2022).
17. Vekstein, A. M. et al. Targeted delivery for cardiac regeneration: comparison of intra-coronary infusion and intra-myocardial injection in porcine hearts. *Front. Cardiovasc. Med.* **9**, 833335 (2022).
18. Yan, R. et al. An enhancer-based gene-therapy strategy for spatiotemporal control of cargoes during tissue repair. *Cell Stem Cell* **30**, 96–111.e6 (2023).
19. Cao, J. & Poss, K. D. The epicardium as a hub for heart regeneration. *Nat. Rev. Cardiol.* **15**, 631–647 (2018).
20. Li, Y., Lua, I., French, S. W. & Asahina, K. Role of TGF-β signaling in differentiation of mesothelial cells to vitamin A-poor hepatic stellate cells in liver fibrosis. *Am. J. Physiol. Gastrointest. Liver Physiol.* **310**, G262–G272 (2016).
21. Keshava, S. et al. The mTORC2/SGK1/NDRG1 signaling axis is critical for mesomesenchymal transition of pleural mesothelial cells and the progression of pleural fibrosis. *Am. J. Respir. Cell Mol. Biol.* https://doi.org/10.1165/rcmb.2023-0131OC (2023).
22. Gajjala, P. R. et al. Wilms tumor 1-driven fibroblast activation and subpleural thickening in idiopathic pulmonary fibrosis. *Int. J. Mol. Sci.* **24**, 2850 (2023).
23. Fischer, A. et al. Post-surgical adhesions are triggered by calcium-dependent membrane bridges between mesothelial surfaces. *Nat. Commun.* **11**, 3068 (2020).
24. Tsai, J. M. et al. Surgical adhesions in mice are derived from mesothelial cells and can be targeted by antibodies against mesothelial markers. *Sci. Transl. Med.* **10**, eaan6735 (2018).
25. Chazarra-Gil, R., van Dongen, S., Kiselev, V. Y. & Hemberg, M. Flexible comparison of batch correction methods for single-cell RNA-seq using BatchBench. *Nucleic Acids Res.* **49**, e42 (2021).
26. Lange, M. et al. CellRank for directed single-cell fate mapping. *Nat. Methods* **19**, 159–170 (2022).
27. Weiler, P., Lange, M., Klein, M., Pe'er, D. & Theis, F. CellRank 2: unified fate mapping in multiview single-cell data. *Nature methods* **21**, 1196–1205 (2024).
28. Fischer, A. et al. In vivo fluorescent labeling and tracking of extracellular matrix. *Nat. Protoc.* **18**, 2876–2890 (2023).
29. Batra, H. & Antony, V. B. Pleural mesothelial cells in pleural and lung diseases. *J. Thorac. Dis.* **7**, 964–980 (2015).
30. Mutsaers, S. E. Mesothelial cells: their structure, function and role in serosal repair. *Respirology* **7**, 171–191 (2002).
31. Zhou, L.-L. et al. Pleural mesothelial cell migration into lung parenchyma by calpain contributes to idiopathic pulmonary fibrosis. *J. Cell. Physiol.* **237**, 566–579 (2022).
32. Zolak, J. S. et al. Pleural mesothelial cell differentiation and invasion in fibrogenic lung injury. *Am. J. Pathol.* **182**, 1239–1247 (2013).
33. Liu, F. et al. Crosstalk between pleural mesothelial cell and lung fibroblast contributes to pulmonary fibrosis. *Biochim. Biophys. Acta Mol. Cell Res.* **1867**, 118806 (2020).
34. Qian, G. et al. DOCK2 promotes pleural fibrosis by modulating mesothelial to mesenchymal transition. *Am. J. Respir. Cell Mol. Biol.* **66**, 171–182 (2022).

35. Järvinen, P. M. et al. Cysteine-rich protein 1 is regulated by transforming growth factor-β1 and expressed in lung fibrosis. *J. Cell. Physiol.* **227**, 2605–2612 (2012).
36. Tantawy, M. A. et al. The interferon-induced gene Ifi27l2a is active in lung macrophages and lymphocytes after influenza a infection but deletion of Ifi27l2a in mice does not increase susceptibility to infection. *PLoS ONE* **9**, e106392 (2014).
37. Savin, I. A., Zenkova, M. A. & Sen'kova, A. V. Pulmonary fibrosis as a result of acute lung inflammation: molecular mechanisms, relevant in vivo models, prognostic and therapeutic approaches. *Int. J. Mol. Sci.* **23**, 14959 (2022).
38. Angelidis, I. et al. An atlas of the aging lung mapped by single cell transcriptomics and deep tissue proteomics. *Nat. Commun.* **10**, 963 (2019).
39. Koga, S. et al. Peripheral PDGFRα+gp38+ mesenchymal cells support the differentiation of fetal liver-derived ILC2. *J. Exp. Med.* **215**, 1609–1626 (2018).
40. Shaikh, H. et al. Fibroblastic reticular cells mitigate acute GvHD via MHCII-dependent maintenance of regulatory T cells. *JCI Insight* **7**, e154250 (2022).
41. Peyser, R. et al. Defining the activated fibroblast population in lung fibrosis using single-cell sequencing. *Am. J. Respir. Cell Mol. Biol.* **61**, 74–85 (2019).
42. Emont, M. P. et al. A single-cell atlas of human and mouse white adipose tissue. *Nature* **603**, 926–933 (2022).
43. McLellan, M. A. et al. High-resolution transcriptomic profiling of the heart during chronic stress reveals cellular drivers of cardiac fibrosis and hypertrophy. *Circulation* **142**, 1448–1463 (2020).
44. Tabula Muris Consortium et al. Single-cell transcriptomics of 20 mouse organs creates a Tabula Muris. *Nature* **562**, 367–372 (2018).
45. Guo, M. et al. Single cell RNA analysis identifies cellular heterogeneity and adaptive responses of the lung at birth. *Nat. Commun.* **10**, 37 (2019).
46. Mederacke, I. et al. The purinergic P2Y14 receptor links hepatocyte death to hepatic stellate cell activation and fibrogenesis in the liver. *Sci. Transl. Med.* **14**, eabe5795 (2022).
47. Bhattacharyya, S. et al. Using Gjd3-CreEGFP mice to examine atrioventricular node morphology and composition. *Sci. Rep.* **9**, 2106 (2019).
48. Byrnes, L. E. et al. Lineage dynamics of murine pancreatic development at single-cell resolution. *Nat. Commun.* **9**, 3922 (2018).
49. Wang, Y. et al. Pulmonary alveolar type I cell population consists of two distinct subtypes that differ in cell fate. *Proc. Natl. Acad. Sci. USA* **115**, 2407–2412 (2018).
50. Mucenski, M. L., Mahoney, R., Adam, M., Potter, A. S. & Potter, S. S. Single cell RNA-seq study of wild type and Hox9,10,11 mutant developing uterus. *Sci. Rep.* **9**, 4557 (2019).
51. Wang, X. et al. Identification of a Zeb1 expressing basal stem cell subpopulation in the prostate. *Nat. Commun.* **11**, 706 (2020).
52. Lukowski, S. W. et al. Single-cell transcriptional profiling of aortic endothelium identifies a hierarchy from endovascular progenitors to differentiated cells. *Cell Rep.* **27**, 2748–2758.e3 (2019).
53. Dahlgren, M. W. et al. Adventitial stromal cells define group 2 innate lymphoid cell tissue niches. *Immunity* **50**, 707–722.e6 (2019).
54. Krentz, N. A. J. et al. Single-cell transcriptome profiling of mouse and hESC-derived pancreatic progenitors. *Stem Cell Rep.* **11**, 1551–1564 (2018).
55. Ziegler, K. A. et al. Immune-mediated denervation of the pineal gland underlies sleep disturbance in cardiac disease. *Science* **381**, 285–290 (2023).
56. Stancill, J. S., Kasmani, M. Y., Khatun, A., Cui, W. & Corbett, J. A. Cytokine and nitric oxide-dependent gene regulation in islet endocrine and nonendocrine cells. *Function* **3**, zqab063 (2022).
57. Balzer, M. S. et al. Single-cell analysis highlights differences in druggable pathways underlying adaptive or fibrotic kidney regeneration. *Nat. Commun.* **13**, 4018 (2022).
58. Konkimalla, A. et al. Multi-apical polarity of alveolar stem cells and their dynamics during lung development and regeneration. *iScience* **25**, 105114 (2022).
59. Schafer, S. et al. IL-11 is a crucial determinant of cardiovascular fibrosis. *Nature* **552**, 110–115 (2017).
60. Hepler, C. et al. Identification of functionally distinct fibro-inflammatory and adipogenic stromal subpopulations in visceral adipose tissue of adult mice. *eLife* **7**, e39636 (2018).
61. Rudman-Melnick, V. et al. Single-cell sequencing dissects the transcriptional identity of activated fibroblasts and identifies novel persistent distal tubular injury patterns in kidney fibrosis. *Res. Sq.* https://doi.org/10.21203/rs.3.rs-2880248/v1 (2023).
62. Thompson, P. J. et al. Targeted elimination of senescent beta cells prevents type 1 diabetes. *Cell Metab.* **29**, 1045–1060.e10 (2019).
63. Kimmel, J. C. et al. Murine single-cell RNA-seq reveals cell-identity- and tissue-specific trajectories of aging. *Genome Res.* **29**, 2088–2103 (2019).
64. Jackson-Jones, L. H. et al. Stromal cells covering omental fat-associated lymphoid clusters trigger formation of neutrophil aggregates to capture peritoneal contaminants. *Immunity* **52**, 700–715.e6 (2020).
65. Long, Y. et al. Deficiency of endothelial FGFR1 alleviates hyperoxia-induced bronchopulmonary dysplasia in neonatal mice. *Front. Pharmacol.* **13**, 1039103 (2022).
66. Narvaez del Pilar, O., Gacha Garay, M. J. & Chen, J. Three-axis classification of mouse lung mesenchymal cells reveals two populations of myofibroblasts. *Development* **149**, dev200081 (2022).
67. Sinton, M. C. et al. IL-17 signalling is critical for controlling subcutaneous adipose tissue dynamics and parasite burden during chronic murine Trypanosoma brucei infection. *Nat. Commun.* **14**, 7070 (2023).
68. Cheng, H.-W. et al. Origin and differentiation trajectories of fibroblastic reticular cells in the splenic white pulp. *Nat. Commun.* **10**, 1739 (2019).
69. Zindel, J. et al. Intraperitoneal microbial contamination drives post-surgical peritoneal adhesions by mesothelial EGFR-signaling. *Nat. Commun.* **12**, 7316 (2021).
70. Strunz, M. et al. Alveolar regeneration through a Krt8+ transitional stem cell state that persists in human lung fibrosis. *Nat. Commun.* **11**, 3559 (2020).
71. Watson, C. K. et al. Antifibrotic drug nintedanib inhibits CSF1R to promote IL-4-associated tissue repair macrophages. *Am. J. Respir. Cell Mol. Biol.* **68**, 366–380 (2023).
72. Parimon, T. et al. Syndecan-1 promotes lung fibrosis by regulating epithelial reprogramming through extracellular vesicles. *JCI Insight* **5**, e129359 (2019). 129359.
73. Peisker, F. et al. Mapping the cardiac vascular niche in heart failure. *Nat. Commun.* **13**, 3027 (2022).
74. Yang, W. et al. Single-cell transcriptomic analysis reveals a hepatic stellate cell-activation roadmap and myofibroblast origin during liver fibrosis in mice. *Hepatoloty* **74**, 2774–2790 (2021).
75. Kostallari, E. et al. Stiffness is associated with hepatic stellate cell heterogeneity during liver fibrosis. *Am. J. Physiol. Gastrointest. Liver Physiol.* **322**, G234–G246 (2022).
76. Tsukui, T. et al. Collagen-producing lung cell atlas identifies multiple subsets with distinct localization and relevance to fibrosis. *Nat. Commun.* **11**, 1920 (2020).
77. Xie, T. et al. Mesenchymal growth hormone receptor deficiency leads to failure of alveolar progenitor cell function and severe pulmonary fibrosis. *Sci. Adv.* **7**, eabg6005 (2021).

78. Habermann, A. C. et al. Single-cell RNA sequencing reveals profibrotic roles of distinct epithelial and mesenchymal lineages in pulmonary fibrosis. *Sci. Adv.* **6**, eaba1972 (2020).
79. Melms, J. C. et al. A molecular single-cell lung atlas of lethal COVID-19. *Nature* **595**, 114–119 (2021).
80. Zhou, X. et al. Microenvironmental sensing by fibroblasts controls macrophage population size. *Proc. Natl. Acad. Sci. USA* **119**, e2205360119 (2022).
81. Liu, X. et al. Categorization of lung mesenchymal cells in development and fibrosis. *iScience* **24**, 102551 (2021).
82. Bischoff, P. et al. The single-cell transcriptional landscape of lung carcinoid tumors. *Int. J. Cancer* **150**, 2058–2071 (2022).
83. Morse, C. et al. Proliferating SPP1/MERTK-expressing macrophages in idiopathic pulmonary fibrosis. *Eur. Respir. J.* **54**, 1802441 (2019).
84. Carraro, G. et al. Transcriptional analysis of cystic fibrosis airways at single-cell resolution reveals altered epithelial cell states and composition. *Nat. Med.* **27**, 806–814 (2021).
85. Delorey, T. M. et al. COVID-19 tissue atlases reveal SARS-CoV-2 pathology and cellular targets. *Nature* **595**, 107–113 (2021).
86. Uhlitz, F. et al. Mitogen-activated protein kinase activity drives cell trajectories in colorectal cancer. *EMBO Mol. Med.* **13**, e14123 (2021).
87. Koenig, A. L. et al. Single-cell transcriptomics reveals cell-type-specific diversification in human heart failure. *Nat. Cardiovasc. Res.* **1**, 263–280 (2022).
88. Ma, L. et al. Tumor cell biodiversity drives microenvironmental reprogramming in liver cancer. *Cancer Cell* **36**, 418–430.e6 (2019).
89. Habenicht, L. K. L. et al. The C1q-ApoE complex: a new hallmark pathology of viral hepatitis and nonalcoholic fatty liver disease. *Front. Immunol.* **13**, 970938 (2022).
90. Parikh, K. et al. Colonic epithelial cell diversity in health and inflammatory bowel disease. *Nature* **567**, 49–55 (2019).
91. Massier, L. et al. An integrated single cell and spatial transcriptomic map of human white adipose tissue. *Nat. Commun.* **14**, 1438 (2023).
92. Chou, E. L. et al. Aortic cellular diversity and quantitative genome-wide association study trait prioritization through single-nuclear RNA sequencing of the aneurysmal human aorta. *Arterioscler. Thromb. Vasc. Biol.* **42**, 1355–1374 (2022).
93. Si, M. et al. Inhibition of hyperglycolysis in mesothelial cells prevents peritoneal fibrosis. *Sci. Transl. Med.* **11**, eaav5341 (2019).
94. Busslinger, G. A. et al. Human gastrointestinal epithelia of the esophagus, stomach, and duodenum resolved at single-cell resolution. *Cell Rep.* **34**, 108819 (2021).
95. Kim, N. et al. Single-cell RNA sequencing demonstrates the molecular and cellular reprogramming of metastatic lung adenocarcinoma. *Nat. Commun.* **11**, 2285 (2020).
96. Reyfman, P. A. et al. Single-cell transcriptomic analysis of human lung provides insights into the pathobiology of pulmonary fibrosis. *Am. J. Respir. Crit. Care Med.* **199**, 1517–1536 (2019).
97. Watanabe, N. et al. Anomalous epithelial variations and ectopic inflammatory response in chronic obstructive pulmonary disease. *Am. J. Respir. Cell Mol. Biol.* **67**, 708–719 (2022).
98. Hao, Y. et al. Integrated analysis of multimodal single-cell data. *Cell* **184**, 3573–3587.e29 (2021).
99. Lotfollahi, M. et al. Mapping single-cell data to reference atlases by transfer learning. *Nat. Biotechnol.* **40**, 121–130 (2022).
100. Young, M. D. & Behjati, S. SoupX removes ambient RNA contamination from droplet-based single-cell RNA sequencing data. *GigaScience* **9**, giaa151 (2020).
101. McGinnis, C. S., Murrow, L. M. & Gartner, Z. J. DoubletFinder: doublet detection in single-cell RNA sequencing data using artificial nearest neighbors. *Cell Syst.* **8**, 329–337.e4 (2019).
102. Bergen, V., Lange, M., Peidli, S., Wolf, F. A. & Theis, F. J. Generalizing RNA velocity to transient cell states through dynamical modeling. *Nat. Biotechnol.* **38**, 1408–1414 (2020).
103. Fang, Z., Liu, X. & Peltz, G. GSEApy: a comprehensive package for performing gene set enrichment analysis in Python. *Bioinformatics* **39**, btac757 (2023).
104. Badia-i-Mompel, P. et al. decoupleR: ensemble of computational methods to infer biological activities from omics data. *Bioinforma. Adv.* **2**, vbac016 (2022).
105. Aibar, S. et al. SCENIC: single-cell regulatory network inference and clustering. *Nat. Methods* **14**, 1083–1086 (2017).
106. Gillespie, M. et al. The reactome pathway knowledgebase 2022. *Nucleic Acids Res.* **50**, D687–D692 (2022).
107. Gene Ontology Data Archive. https://doi.org/10.5281/zenodo.7504797.

Acknowledgements

We thank Dr. Sibylle Sabrautzki for her veterinary advice and support. This project was supported by the European Research Council Consolidator Grant (ERC-CoG 819933) and the LEO Foundation (LF-OC-21-000835). Figures were created with BioRender.com.

Author contributions

Y.R. outlined and supervised the research narrative and experimental design. S.K. analyzed the scRNAseq data, performed image analysis, ex-vivo and in-vivo experiments, and designed the figures and schematics. A.F. and W.H. performed immunohistochemistry, in-vivo bleomycin experiments, and image analysis. M.M. generated and validated all the AAV for the study. A.K. analyzed scRNAseq data and performed immunostaining. L.Y., Y.L., W.H., S.H., H.Y. performed immunostaining and ex-vivo experiment. P.R. performed imaging. M.A. & H.S. generated the mouse scRNAseq libraries and assisted with data analysis. H.-G.M. assisted with translational and clinical advice. Y.R. and S.K. wrote and revised the manuscript with W.H., A.F., and M.M. support.

Competing interests

The authors declare the following competing interests: A.F., M.M., S.K., and Y.R. have filed patent application WO2023079127A1 covering the use of these methods to study and manipulate mesothelial cells in lung fibrosis. The remaining authors declare no competing interests.

Additional information

Supplementary information The online version contains supplementary material available at https://doi.org/10.1038/s41467-025-63990-2.

Correspondence and requests for materials should be addressed to Wei Han or Yuval Rinkevich.

Peer review information *Nature Communications* thanks the anonymous reviewer(s) for their contribution to the peer review of this work. A peer review file is available.